Monthly Notices
of the
ROYAL ASTRONOMICAL SOCIETY

MNRAS **507,** 5523–5541 (2021)
Advance Access publication 2021 August 13

https://doi.org/10.1093/mnras/stab2311

Axisymmetric simulations of the convective overstability in protoplanetary discs

Robert J. Teed [1,2]★ and Henrik N. Latter[2]

[1]*School of Mathematics and Statistics, University of Glasgow, University Place, Glasgow G12 8SQ, UK*
[2]*DAMTP, University of Cambridge, CMS, Wilberforce Road, Cambridge CB3 0WA, UK*

Accepted 2021 August 1. Received 2021 July 27; in original form 2021 April 12

ABSTRACT

Protoplanetary discs at certain radii exhibit adverse radial entropy gradients that can drive oscillatory convection ('convective overstability'; COS). The ensuing hydrodynamical activity may reshape the radial thermal structure of the disc while mixing solid material radially and vertically or, alternatively, concentrating it in vortical structures. We perform local axisymmetric simulations of the COS using the code SNOOPY, showing first how parasites halt the instability's exponential growth, and secondly, the different saturation routes it takes subsequently. As the Reynolds and (pseudo-) Richardson numbers increase, the system moves successively from (i) a weakly non-linear state characterized by relatively ordered non-linear waves, to (ii) wave turbulence, and finally to (iii) the formation of intermittent and then persistent zonal flows. In three dimensions, we expect the latter flows to spawn vortices in the orbital plane. Given the very high Reynolds numbers in protoplanetary discs, the third regime should be the most prevalent. As a consequence, we argue that the COS is an important dynamical process in planet formation, especially near features such as dead zone edges, ice lines, gaps, and dust rings.

Key words: accretion, accretion discs – convection – instabilities – turbulence – protoplanetary discs.

1 INTRODUCTION

For most of their lives, protoplanetary (PP) discs are too cold and poorly ionized to support a form of the magnetorotational instability unhindered by non-ideal MHD (e.g. Turner et al. 2014). This state of affairs has renewed interest in the ability of purely hydrodynamic processes to supply the turbulent activity necessary for disc accretion (Lesur & Fromang 2019; Lyra & Umurhan 2019). Indeed, a number of hydrodynamic instabilities may attack discs at certain radii and at certain evolutionary stages; the most commonly discussed are the vertical shear instability (VSI), the Rossby wave instability, the subcritical baroclinic instability, and radial oscillatory convection (also called 'convective overstability'; COS) (e.g. Urpin and Brandenburg 1997; Lovelace et al. 1999; Lesur and Papaloizou 2009; Klahr and Hubbard 2014; Lyra 2014). These instabilities, however, produce flows that are probably too weak to solve the problem of angular momentum transport, though they may be important for dust diffusion and aggregation. In fact, observations in scattered light and the (sub-) mm do suggest only a mild level of background turbulence: sufficient to loft small μm dust, yet unable to stir up larger mm-sized grains (e.g. Perrin et al. 2009; Pinte et al. 2016). This low-level activity is also consistent with recently measured turbulent broadening of molecular lines (Flaherty et al. 2015, 2017, 2018).

Ordinarily, a negative radial entropy gradient is stabilized by a disc's strong angular momentum gradient (cf. the Solberg-Høiland criterion; Tassoul 2000). But if cooling is not too strong nor too weak a form of oscillatory double-diffusive convection, the COS, finds a way around this constraint and produces hydrodynamical activity (Latter 2016, hereafter L16). Actually, most PP discs possess a positive entropy gradient on average (L16), though more recent observations indicate there is a significant subset that bucks this trend (de Gregorio-Monsalvo et al. 2013; Tazzari et al. 2017). In any case, all discs should undergo sharp transitions at special radii, such as dead zone edges, ice lines, gaps, and dust rings where it is likely a strongly decreasing entropy profile might develop. It is the goal of this paper to assess the behaviour and vigour of the COS in such special regions.

Earlier work has shown that COS modes cannot grow too large before being attacked by parasitic instability (L16). If the parasites set the level of hydrodynamic activity, then the COS saturates at a relatively low level. But it is also possible that, after its initial breakdown, the turbulent flow splits into a sequence of zonal flows, by analogy with semiconvection, thus leading to a far more vigorous and interesting state (Rosenblum et al. 2011; Zaussinger and Spruit 2013). These flows, in turn, may be subject to Kelvin-Helmholtz instability and hence will shed vortices that could accumulate solids (Lyra 2014; Raettig et al. 2021).

To understand the saturation properties of the COS, and in particular its propensity to form zonal flows, we undertake axisymmetric simulations in the Boussinesq shearing box with SNOOPY, a commonly used pseudo-spectral code (Lesur and Longaretti 2005). We traverse a range of parameters, primarily the Reynolds and (pseudo-) Richardson numbers (Re and R, respectively), to determine the various non-linear outcomes available to the system.

★ E-mail: Robert.Teed@glasgow.ac.uk

We find that at low Re and R, the system exhibits laminar non-linear wave states that can be modelled by a simple dynamical system based on a three-wave resonance (e.g. Craik 1985). Increasing either Re or R sees the system enter a 'wave-turbulent' state, comprised of a disordered field of inertial waves (e.g. Galtier 2003). At larger values of Re and R, this state supports additional vertical elevator modes and the intermittent formation of zonal flows via a mean-field antidiffusive instability, similar in nature to the layer formation witnessed in thermohaline and semiconvection (e.g. Rosenblum et al. 2011; Traxler et al. 2011; Mirouh et al. 2012; Spruit 2013; Zaussinger and Spruit 2013), and also jet production in turbulent planetary atmospheres and tokamak plasmas (e.g. Diamond et al. 2005; Dritschel and McIntyre 2008). For higher Re and R the zonal flows persist and strengthen. We expect these flows to generate vortices in the orbital plane when the restriction of axisymmetry is lifted. We delineate the boundaries between these different saturation regimes in the Re-R parameter space, and argue that if the COS is to appear on reasonable time-scales it is the persistent zonal flow regime that is most likely in PP discs.

The paper is organized as follows. In Section 2, we briefly outline the background physics of the COS and discuss its prevalence in PP discs, while Section 3 presents the tools we employ to understand it: the model equations and their numerical implementation. Our results appear in Sections 4 and 5, where first we examine the onset and initial breakdown of the instability, making comparison with previous work, and second describe the subsequent evolutionary paths the system might take and their dependence on the physical parameters. In Section 6, we outline a model that helps explain why zonal flows form. Conclusions are drawn and future work pointed out in Section 7.

2 BACKGROUND

2.1 Instability mechanism and basic properties

We begin by briefly describing the physical cause of instability. In essence, the fastest growing COS mode is an epicycle accompanied by a thermodynamic oscillation. If thermal diffusion is present, a crucial time-lag develops between the dynamical component of the oscillation (the epicycle) and the thermodynamic component. This means that after half an epicycle a fluid blob returns to its starting radius with a different temperature than that which it started (and hence its immediate surroundings at that instant). In the presence of a negative radial entropy gradient, the blob will hence suffer a buoyancy acceleration that amplifies the initial oscillation and leads to runaway growth. For more details see Section 3.3 in L16.

Note that the instability condition is the Schwarzschild criterion, rather than the Solberg–Høiland criterion: the COS has found a way to use thermal diffusion to negate the stabilizing influence of rotation. As with many hydrodynamical instabilities in accretion discs, the COS is 'double diffusive', relying on thermal diffusion, in this case, to vastly overwhelm viscous diffusion. A final point is that the instability mechanism is similar to the subcritical baroclinic instability (SBI; Klahr & Bodenheimer 2003; Petersen et al. 2007; Lesur and Papaloizou 2010), but we emphasize the two instabilities are distinct. The COS is linear and axisymmetric and requires a vertical wavenumber ($k_z \neq 0$), while the SBI is non-linear and non-axisymmetric and works in razor-thin discs (where there is no k_z).

Other key COS properties include its maximum growth rate and characteristic length scale. The former reaches $-(1/4)(N^2/\kappa)$, where N^2 is the squared radial buoyancy frequency and κ is the epicyclic frequency. If radiative cooling is described in the diffusive approximation, maximum growth occurs on a distinct wavelength $\approx \sqrt{\xi/\kappa}$, where ξ is thermal diffusivity. Typically this length scale is longer than the photon mean free path in the inner radii of typical PP disc models (see Table 1), and thus the diffusive approximation is acceptable, certainly for linear analyses, and probably for non-linear simulations.

Table 1. Properties of the minimum mass PP disc of Chiang & Youdin (2010) at three different radii. Symbols are defined in Sections 3.1 and 3.2. The Reynolds number is calculated assuming Pe=$4\pi^2$, thus taking $L = \lambda_{\max}$.

Radius (AU)	1	5	10
H (cm)	3.3×10^{11}	2.6×10^{12}	6.4×10^{12}
$\ell_{\rm mfp}$ (cm)	1.3×10^{8}	4.6×10^{10}	5.7×10^{11}
$\lambda_{\max}$ (cm)	10^{9}	2.1×10^{11}	2.1×10^{12}
$\lambda_{\rm crit}$ (cm)	10^{8}	7.5×10^{9}	4.8×10^{10}
$\ell_{\rm visc}$ (cm)	7.8×10^{4}	7.4×10^{5}	1.9×10^{6}
Re	6.4×10^{7}	4.0×10^{9}	2.4×10^{10}

2.2 Prevalence in PP discs

Early observations in the (sub-) mm continuum permitted researchers to infer the large-scale (smooth) radial profiles of PP disc temperatures, densities, etc. (e.g. Andrews et al. 2009; Isella et al. 2009; Guilloteau et al. 2011). Generally, they indicated that most discs possess a positive entropy gradient, on account of the surface density's steep fall-off with radius, thus suggesting that discs were stable (in bulk) to the COS (see Sections 8.2 in Lin & Youdin 2015 and 3.4.1 in L16). However, the high angular resolution afforded by ALMA, especially, has shown that, within 100 AU, PP discs exhibit far flatter surface-density profiles than previously thought. In fact (within the modelling errors) HD 163296 and several examples in Lupus (e.g. Sz 65, Sz 71, and Sz 98), possess almost no variation in surface density at 10s of AU, while a number of other discs see their surface densities gently increase (de Gregorio-Monsalvo et al. 2013; Tazzari et al. 2017). The COS's chances are much improved in such environments, though it still very much depends on the large-scale temperature profile and the degree of flaring (L16). We conclude that there are probably a significant subset of PP discs that support the COS throughout a broad range of radii between 1 and 10 AU.

On the other hand, PP discs exhibit a great deal of complicated and sometimes abrupt radial structure. Multiple observations reveal gaps, dust rings, and spirals, while theory posits special radii such as ice lines and dead/active zone boundaries (e.g. Gammie 1996; Lecar et al. 2006; Armitage 2011; Muto et al. 2012; Brogan et al. 2015; Fedele et al. 2017). It is conceivable that around such features the entropy gradient will flip, especially if these regions suffer radially inhomogeneous heating, as might be expected at the inner dead-zone edge, at the outer edge of a ring or gap, or in regions shielded from the central star by vertical disc deformations (e.g. Chrenko and Nesvorny 2020, Dullemond et al. 2001, Natta et al. 2001, Jankovic et al. 2021). On the other hand, sublimation/condensation fronts and opacity transitions can display abrupt 'thermal anomolies' and associated entropy jumps (e.g. Garaud and Lin 2007). We might expect the COS to appear in these localized pockets, and perhaps to best function on account of the stronger local gradients. These regions will then be reshaped, thanks to the COS, via mixing of both heat and solid particles.

Separate to the observations, theoretical models of global disc structure have attempted to answer the question of the prevalence and location of instabilities such as the COS. Models based on passively

irradiated discs generally admit stable radial entropy profiles, unless the surface density varies very slowly; work using such set-ups have investigated cooling rates and their impact on instability, but cooling rates alone cannot decide whether the COS grows or not, and are hence potentially misleading (e.g. Malygin et al. 2017; Lyra & Umurhan 2019). 'Active' alpha-disc models, on the other hand, can yield radial intervals in which the entropy gradient becomes negative and the COS unstable (Pfeil & Klahr 2019). But then what is supplying the 'alpha', if not the COS itself? If this background heating issues from a separate source of turbulence, will this not interfere with the emergence of the COS? Furthermore, the vertical profile of heat deposition may not be in accord with an alpha-type viscosity (see for example Mori et al. 2019). Clearly, the theoretical models need further work. For the moment, we simply posit that the COS can prevail in a subset of PP discs, possibly on a range of radii or in isolated pockets associated with abrupt structure.

2.3 Saturation, zonal flows, and elevator flows

To assess the influence of the COS, we must track its non-linear evolution. L16 showed that the fastest growing modes are attacked by a parametric instability involving a three-way resonance with inertial waves. Typically these limit the initial saturation amplitude of the COS to relatively low levels, with random velocities some 10^{-5} the local sound speed, probably too low to be of interest. However, for certain parameters, the subsequent evolution of the turbulence may be quite different, breaking it up into radial layers of strong stratification in temperature and angular momentum accompanied by much stronger velocities and transport. In fact, this is what is seen in some of the simulations of axisymmetric COS by Lyra (2014) and of 2D semiconvection, which is mathematically identical (Rosenblum et al. 2011; Mirouh et al. 2012). In full 3D, these layers, or rather 'zonal flows', could shed vortices via Kelvin-Helmholtz instability. This is an outcome of much greater interest as it is likely to impact not only on the disc structure but on particle accumulation and even planet formation.

The emergence of zonal flows is, in fact, generic to turbulent and rotating systems. They are witnessed not only in planetary atmospheres and tokamaks, but in several accretion disc context: simulations of the MRI (Steinacker and Papaloizou 2002, Johansen et al 2009; Simon et al. 2012; Kunz and Lesur 2013), the parametric instabilities that afflict eccentric discs (Wienkers & Ogilvie 2018), and the VSI (Richard et al. 2016). Moreover, the geostrophic balance, underlying zonal flows, controls the linear instability mechanism of several disc processes: the VSI itself (Latter & Papaloizou 2018), the streaming instability (Jacquet et al. 2011), the secular dust gravitational instability (Latter & Rosca 2017), the diffusive gravitational instability (Vanon & Ogilvie 2017), and the double-diffusive resistive instability (Latter et al. 2010).

Geostrophic balance comprises a quasi-steady equilibrium between the Coriolis force and the pressure gradient (alongside, possibly, radial buoyancy or Lorentz forces), which naturally produces a radial sequence of super and sub-Keplerian jets (zonal flows). In the absence of viscosity, these jets form by a non-linear process that 'swaps' rings of material at different radii: the outer ring moves in and orbits slower than the material immediately surrounding it, while the inner ring moves out and rotates faster. The two rings are held in place by pressure, otherwise they would fall back to whence they came (via the Coriolis force). Note that zonal flows need not arise from exchange of angular momentum between fluid rings, but from exchange of radial location. This is important because in (inviscid) axisymmetry no angular momentum exchange is possible.

The obvious question is how these swaps can be arranged by the turbulent flow. In geophysics, it is common to invoke a mean-field antidiffusive instability (e.g. the 'zonostrophic' and 'gamma' instabilities; Radko 2003; Srinivasan and Young 2012); in 2D semiconvection, Garaud and coworkers have shown that simple turbulence closure models based on these ideas are consistent with numerical simulations (Rosenblum et al. 2011; Stellmach et al. 2011; Traxler et al. 2011; Mirouh et al. 2012; Wood et al. 2013). However, the physical insight obtained is somewhat limited and, moreover, the mean field models are not predictive and can only be deployed in the post-processing of numerical data. Alternatively, the development of such flows has been explored directly from the system's underlying non-linear wave couplings: though in ideal hydrodynamics a three-wave coupling is incapable of generating geostrophic modes (Greenspan 1969), higher order resonant interactions might be able to, as could the introduction of irreversibility via an instability (such as provided by the COS, or possibly the VSI), dissipation, turbulence, or even the detuning of a wave triad (e.g. Smith and Waleffe 1999, Kerswell 1999, Le Reun et al. 2020).

In this paper, we take the former approach and build a physical mean-field model to aid our intuition of the antidiffusive behaviour, based on the local angular momentum fluxes generated by forced inertial waves. Because the wave forcing (from the COS) is itself sensitive to the angular momentum gradient, the possibility of up-gradient angular momentum transport (hence antidiffusion) can be brought out in a relatively transparent way.

Finally, we acknowledge that vertically local disc models (including cylindrical discs; Dewberry et al. 2020) often develop elevator flows, which usually consist of a radial sequence of updrafts and downdrafts exhibiting no vertical variation (see for example, Calzavarini et al. 2006), and some of our COS simulations are no exception. They may be interpreted as attempts by the system to manifest a larger scale circulation, and thus are not unphysical necessarily, but are certainly poorly described by local models.

3 GOVERNING EQUATIONS AND NUMERICAL METHODS

3.1 Equations and parameters

Being interested in small scales and subsonic flow, we employ the Boussinesq shearing box (Latter & Papaloizou 2017, hereafter LP17). This model describes a small 'block' of disc centred upon a cylindrical radius r_0 moving on the circular orbit prescribed by r_0 and at an orbital frequency of Ω. We are also free to stipulate the vertical height of the block, z_0, above the midplane, though throughout we assume $z_0 = 0$. The block is represented in Cartesian coordinates with the x and y directions corresponding to the radial and azimuthal directions, respectively (see Goldreich & Lynden-Bell 1965). The model can include both vertical and radial stratification, as well as vertical shear, but to keep things simple we incorporate only radial stratification – a necessary ingredient for the COS. Future work might explore the interplay between the COS and other physics – and indeed the VSI, if present. We stress that the Boussinesq shearing box equations can be derived self-consistently and do not rely on any ad-hoc or problematic assumptions.[1]

The governing equations are

[1]This is in contrast to recent work using compressible local frameworks and an explicit radial pressure gradient (e.g. Lyra and Klahr 2011), which can be marred by spurious overstabilities (LP17).

$$\partial_t \mathbf{u} + \mathbf{u}\cdot\nabla\mathbf{u} = -\frac{1}{\rho}\nabla P - 2\Omega\mathbf{e}_z \times \mathbf{u} + 2q\Omega\, x\, \mathbf{e}_x - N^2\theta\, \mathbf{e}_x + \nu\nabla^2\mathbf{u}, \quad (1)$$

$$\partial_t\theta + \mathbf{u}\cdot\nabla\theta = u_x + \xi\,\nabla^2\theta, \quad (2)$$

$$\nabla\cdot\mathbf{u} = 0, \quad (3)$$

where $\mathbf{u}$ is the fluid velocity, P is pressure, ρ is the (constant) background density, θ is the buoyancy variable. The dimensionless shear parameter of the sheet is denoted by q, equal to (3/2) in a Keplerian disc, and the buoyancy frequency arising from the radial stratification is denoted by N. We employ thermal diffusion rather than an optically thin cooling law, as is done in Klahr & Hubbard (2014) and Lyra (2014), with ξ the thermal diffusivity.[2] Viscous diffusion is also included, with ν the kinematic viscosity, understood to be molecular.

The (squared) buoyancy frequency can be determined from

$$N^2 = -\frac{1}{\gamma\rho}\frac{\partial P}{\partial r}\frac{\partial \ln\left(P\rho^{-\gamma}\right)}{\partial r}, \quad (4)$$

evaluated at $r = r_0$. In the above γ is the adiabatic index. Another important quantity is the (squared) epicyclic frequency

$$\kappa^2 = 2(2-q)\Omega^2, \quad (5)$$

which describes the angular momentum structure of the disc.

Following Lesur & Papaloizou (2010), the stratification length has been absorbed into θ, so that $\theta = -(\partial_R S)_0^{-1} S'$, where S' is the dimensionless entropy perturbation. The total entropy in the box may then be associated with the quantity $\theta_x = -x + \theta$. On the other hand, the total angular momentum is $h = 2\Omega x + u_y$ (LP17).

In addition to q, the system can be specified by three other dimensionless parameters. The 'R' number measures the relative strength of the (unstable) radial stratification to the stabilizing angular momentum gradient:

$$R = -\frac{N^2}{\kappa^2}. \quad (6)$$

In some previous work, this has been (incorrectly) identified with the Richardson number, which instead possess the squared shear rate in the denominator. Though the distinction is unimportant in most contexts, we emphasize that the COS is sensitive to the angular momentum gradient, not the shear rate per se; and when explaining layer formation (which is caused by radial variations in R) this is a key point. In thin astrophysical discs, we might expect R to be small, as discussed in L16. (Note that R is denoted by n^2 in L16 .)

Finally, the relative importance of the diffusivities is measured by the Peclet and Reynolds numbers

$$\mathrm{Pe} = \frac{L^2\kappa}{\xi}, \qquad \mathrm{Re} = \frac{L^2\kappa}{\nu}, \quad (7)$$

where L is a characteristic outer length scale. Our model has no intrinsic physical outer scale, so L must be taken to be our box size. Please be aware that our Pe and Re do not correspond to the usual definitions, because L need not be H the disc scale height. Lastly, we occasionally make use of the Prandtl number, $\mathrm{Pr} = \nu/\xi$.

[2]An unnerving consequence of the adoption of a single cooling time in local models of the COS is that the $k = 0$ mode grows; i.e. the box itself is unstable! (See equation 21 in Lyra 2014.)

3.2 Characteristic length scales

To get a feel for the physical scales in our problem we adopt a specific disc model, a minimum-mass solar nebula developed by Chiang & Youdin (2010) and Lin & Youdin (2015). This provides scaling laws for relevant midplane properties. For example, in cgs units,

$$\Sigma = 2200\, r_{\mathrm{AU}}^{-3/2},\ H = 3.3\times10^{11}\, r_{\mathrm{AU}}^{9/7},\ \ell_{\mathrm{mfp}} = 1.3\times10^{8}\, r_{\mathrm{AU}}^{51/14},$$

where Σ is the surface density, ℓ_{mfp} is the photon mean free path, and r_{AU} is disc radius in AU.

In addition, we can estimate the wavelength of fastest COS growth $\lambda_{\mathrm{max}} \approx \sqrt{\xi/\kappa}$, and the critical wavelength below which the linear instability switches off, λ_{crit} (cf. equation (A2) in Latter 2016 [3]):

$$\lambda_{\mathrm{max}} = 10^9\, r_{\mathrm{AU}}^{93/28}, \qquad \lambda_{\mathrm{crit}} = 10^8\left(\frac{R}{0.01}\right)^{-1/4} r_{\mathrm{AU}}^{75/28}.$$

Notice the very weak scaling with R in our expression for λ_{crit}. In the following discussion we omit this factor: values of R any less than 10^{-3} produce linear COS growth times too small to be important (greater than $10^4\,\Omega^{-1}$).

On length scales shorter than λ_{crit}, we expect the COS to instigate a direct turbulent cascade, which ultimately approaches the isotropic Kolmogorov regime (Nazarenko & Schekochihin 2011, LP17). Kinetic energy will be thermalized on the Kolmogorov dissipation length $\ell_{\mathrm{visc}} = (\nu^3/\varepsilon)^{1/4}$, where ε is the (specific) energy injection rate, equal to $N^2\langle\theta u_x\rangle$ in our problem, with the angle brackets denoting a suitable length and time average. Assuming a quasi-linear approach, by setting the relevant injection length and time-scales to be those of the fastest growing mode (λ_{max} and Ω) we obtain $\varepsilon \sim \xi|N^2|$, and find simply

$$\ell_{\mathrm{visc}} \sim \mathrm{Pr}^{1/2}\lambda_{\mathrm{crit}}.$$

We caution that the quasi-linear approximation fails when large-scale structures appear, such as elevator and zonal flows, in which case ℓ_{visc} will be shorter (see discussion in Section 5.3). It is, however, a useful first estimate.

In Table 1, we list these characteristic length scales at selected disc radii for reference. Within about 5 AU, the COS length scales are significantly less than H thus justifying the vertically unstratified approximation. Further out, however, this becomes increasingly a problem. On the other hand, for $r < 10$ AU the main COS injection scale λ_{max} always lies above the photon mean free path. While the inertial range of the turbulent cascade does fall within the optically thin regime, radiative physics is unimportant for the cascade. Together this justifies our use of the diffusion approximation. We stress, however, that these estimates are tied to a specific, rather massive, disc model: a 'lighter' disc (such as the template used in Lesur & Latter 2016) may find ℓ_{mfp} and λ_{max} comparable. Perhaps more importantly: the surface density in our fiducial nebula falls off far more steeply than the observed discs discussed in Section 2.2, especially those most susceptible to the COS. The number generated here are thus only illustrative and certainly not definitive.

3.3 Numerical methods

3.3.1 Code and set-up

We perform numerical simulations with the code, SNOOPY (Lesur & Longaretti 2005, 2007), which solves the shearing box equations

[3]This equation suffers from a typo: ξ^2/κ^2 should be replaced by κ^2/ξ^2. There are also a handful of other unfortunate instances in L16 where this ratio is inverted.

using a pseudo-spectral method based on a shearing wave decomposition. As we only calculate axisymmetric flow, the wavevectors do not depend on time, and no remapping is required. Non-linear terms are computed in real space, but a 2/3 aliasing rule is imposed in spectral space. The time integration of non-diffusive terms is undertaken by the explicit third-order Runge–Kutta method, while the diffusive terms are integrated by an implicit procedure.

We employ a rectangular domain of size $L_x \times L_z$. Typically $L_x = 2L_z = 2L$. Our basic simulations employ a grid of 512 × 256 units. Note that, being spectral, SNOOPY develops hatched saw-tooth structure on the grid-scale if a simulation is under-resolved (related to the Gibbs phenomenon); though this does not always crash the run it is easy to detect, and when we do see it we stop the simulation and rerun it at a higher resolution.

The domain is periodic in both x and z. Units are chosen so that $L = 1$, $\Omega = 1$, and $\rho = 1$. Simulations are normally initialized with white noise of a given amplitude, or otherwise with an exact COS mode sometimes polluted with smaller amplitude white noise.

3.3.2 *Parameter values*

In all runs, the disc is Keplerian and so $q = 3/2$, which leaves three dimensionless parameters: R, Pe, and Re. Roughly speaking, the greater the R and Re, the faster growing the instability and the more vigorous the ensuing activity. We mainly vary R and Re, though to 'speed up' the simulations we generally take a large value of R, setting it often to 0.1. In reality, the thermal gradient could vary greatly depending on the radial structure that generated it. This is our principal unknown.

The Peclet number, Pe, sets the thermal length (and $\lambda_{\rm max}$) with respect to the box size L. Thus, indirectly, Pe also controls the box size relative to the disc scale height. In almost all runs we let Pe$=4\pi^2 \approx 40$, which means the vertical size of the box is the same as that of the fastest growing COS mode, i.e. $L = 2\pi\sqrt{\xi/\Omega} = \lambda_{\rm max}$. By setting the energy input scale near the box size, we allow ourselves the dynamical range to set realistic (molecular) Re. The downside is that coherent large-scale structures near the input scale or larger will be impacted upon by the numerical domain. Future work might compromise on the viscous scales, but set the box size much larger so as to mitigate such effects.

We let the Reynolds number in our simulations range between 10^3 and 10^7. Given a global disc model (such as in Section 3.2) we can relate L to H, the disc semithickness. Then, by fixing Pe$=4\pi^2 \approx 40$, we can determine our Re as a function of disc radius (noting that it differs from the usual definition by a factor $(H/L)^2$). Representative values for Re are placed in Table 1. We see that the Reynolds number at 1 AU is just within the range achievable by our simulations. Beyond 1 AU, however, the Reynolds number increases beyond what is numerically possible. These limitation should be kept in mind when interpreting our results.

Finally, for given R and Pe, there is a critical Reynolds number $\mathrm{Re_c}$ below which the instability switches off entirely in our simulations. This critical value can be obtained by setting $\lambda_{\rm crit}$, the marginal wavelength, to L, which yields a cubic for Re. For example, when $R = 0.1$ and Pe$=4\pi^2$ then we have $\mathrm{Re}_c \approx 1580$. A rough but useful approximation, assuming small Pr, is $\mathrm{Re}_c \approx 2^5\pi^4/(\mathrm{Pe}\,R)$.

3.3.3 *Diagnostics*

Our main diagnostics are

$$E_K = \langle\rho|\mathbf{u}|^2\rangle, \qquad F_H = \langle u_x u_y'\rangle, \qquad F_\theta = \langle u_x\theta\rangle, \tag{8}$$

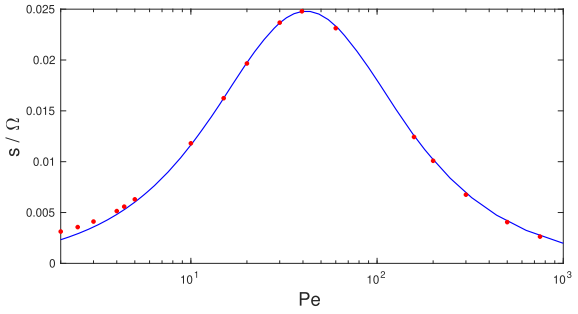

Figure 1. Linear growth rate of the COS mode s as a function of Pe, for $R = 0.1$ and Re$=2 \times 10^5$. The solid blue curve represents the analytic solution; the red dots are numerically calculated values.

representing the box-averaged kinetic energy, angular momentum flux, and heat flux, respectively. Here the angle brackets now signify an average over the spatial domain, and u_y' is the deviation from the background differential rotation. As SNOOPY is a spectral code, the spatial integrations can be undertaken conveniently in spectral space, via Parseval's theorem. Note that 'alpha' parameters can be constructed from F_H and F_θ; using our system of units we obtain the classical $\alpha = (L^2/H^2)F_H$, for instance. We also make use of the directional kinetic energies $E_{Kx} = \langle\rho u_x^2\rangle$, $E_{Ky} = \langle\rho(u_y')^2\rangle$, and $E_{Kz} = \langle\rho u_z^2\rangle$.

It is possible to pick out the various spectral components of a field (indexed by their radial and vertical wavenumber) and to plot the associated power. Thus, for example, $\widetilde{u}_x^{mn}$ represents the Fourier coefficient of u_x with the m'th radial wavevector and n'th vertical wavenumber. The power in a mode is the modulus square of its associated coefficient.

4 ONSET OF THE CONVECTIVE OVERSTABILITY

4.1 Growth rates

We begin by testing the numerical code against the linear theory of the COS. We do this by comparing the numerical linear growth rates from SNOOPY to those predicted by L16. The simulations are initialized with a clean COS eigenfunction. By keeping L fixed and the wavevector of the mode $=2\pi/L$, when we vary the Peclet number we can effectively sample the COS dispersion relation; this is because the growth rate s depends on $k_z(\xi/\kappa)^{1/2} = (k_z L)\,\mathrm{Pe}^{-1/2}$.

In Fig. 1, the analytical curve and numerical data points are overlaid for the parameters $R = 0.1$ and Re $= 2\times 10^5$. The analytic curve is derived from the viscous dispersion relation, equation (A1) in L16. For most wavenumbers the agreement is excellent (within 1 per cent), but for low Pe (large k_z) the growth rates diverge somewhat. This is because these slower growing modes are usually overtaken by other modes before they can grow appreciably, and thus estimating their growth rates is more error prone.

4.2 Maximum amplitudes

Now we test the parasitic theory of L16 by determining the amplitude of a COS mode at the point that its exponential growth halts. At the same time we track the amplitude of the parasitic modes that attack it. This is achieved by comparing the sizes of the leading Fourier component of u_x and of u_z, as functions of time, in the initial stages of several runs: the former corresponds to the COS, the latter to other

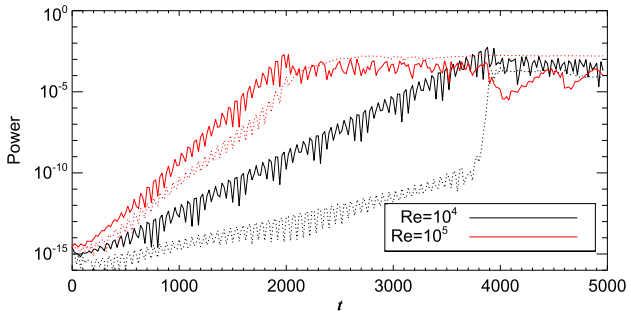

Figure 2. Largest spectral components of u_x (solid) and u_z (dashed) as a function of time for two values of Re ($=10^4$ and 10^5). Both runs have $R = 10^{-1.5}$ and Pe$=4\pi^2$.

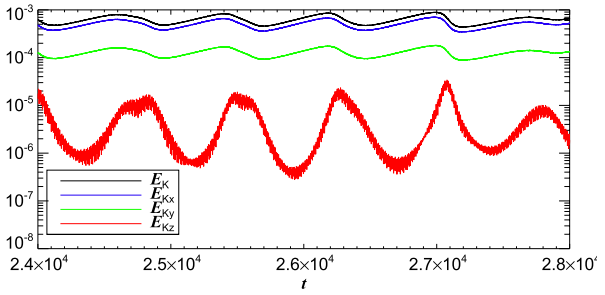

Figure 3. Kinetic energy, and its separate components, as a function of time bandpass filtered to remove highest frequency oscillations. Simulation parameters are $R = 10^{-1.5}$, Pe$=4\pi^2$, Re$=10^{3.75}$.

inertial waves, including the parasites. It is possible to distinguish the two modes this way because the fastest growing COS (the primary) possesses no vertical velocity in its eigenfunction, while the parasitic modes do (being inertial waves with $k_x \neq 0$).

First, we find that if the simulation is initialized with a clean COS mode it will grow indefinitely, or at least until the code crashes. This behaviour is in agreement with equation (33) in L16, which states that if the starting amplitude of the parasite is very small (as when seeded by numerical error), then the maximum COS amplitude will be extremely large on account of the divergence of the Lambert W function near the origin.

We next seed the simulations with white noise, from which both the COS and its parasites can emerge. Now, after some time, both grow and saturate at a similar order of magnitude. Fig. 2 demonstrates this behaviour in two simulations performed with different values of the Reynolds number. Power in the COS modes is represented by solid lines, and power in modes with $u_z \neq 0$ by dotted lines. Different colours indicate different Re. In both cases the fastest growing COS mode grows exponentially fast initially, in accord with the linear growth rate, whilst there is some weaker exponential growth amongst the other modes, which we associate with the slower growing COS with $k_x \neq 0$. However, at a critical time, dependent on Re, the primary COS achieves a sufficient amplitude for the parasite's growth rate to shoot up superexponentially, outcompete the primary COS, and ultimately saturate its growth. At larger Re the saturation time occurs sooner, but the final saturated states all possess a similar power. L16 predicts an initial saturated state with kinetic energy $\sim R^2 \sim 10^{-3}$, which provides a good estimate on the peak amplitude at the point of breakdown. Immediately afterwards the flow settles down to a slightly less active level.

5 SATURATED STATES

In this section, we demonstrate the possible long-term outcomes of the system's evolution. The dynamics are parameter dependent and we have identified at least three saturation routes, which are accessed consecutively as R and/or Re increase, i.e. as the system becomes more COS unstable. We introduce these three saturation routes separately along with a discussion of a typical case for each, and then present the results of a parameter sweep showing where in parameter space each state can be found.

5.1 Weakly non-linear regime

At parameter values just above critical for the onset of the instability, the system enters a low-order 'weakly non-linear' regime which is controlled by a small number of modes. For fixed R and Pe, this regime occurs for Re near the critical $\mathrm{Re}_{\mathrm{crit}}$ below which the linear COS fails to appear. If we equate L with H then Re_c is generally too small to apply to real PP discs. But we provide details of this regime for completeness and also because it helps illuminate the dynamics at larger, and more realistic, Re.

Our representative case possesses parameters $R = 10^{-1.5} \approx 0.032$, Pe$=4\pi^2 \approx 40$, Re$=10^{3.75} \approx 5620$, which means the most unstable COS mode has wavelength equal to the vertical domain size L. We find that after saturation the system exhibits two time-scales: the short period of the epicyclic oscillation $\sim\Omega^{-1}$ (associated with the primary COS mode), and a much longer time-scale $\sim 1000\Omega^{-1}$ (of the order of the linear growth time of the COS). In order to bring out the longer variation we impose a band-pass filter to remove the shorter epicyclic frequency, and plot the filtered energies in Fig. 3 on an interval of size $4 \times 10^3\ \Omega^{-1}$, well after the initial saturation and any transients associated with it.

The first thing to note is that the energy is dominated by the horizontal components, and that the radial energy is roughly four times larger than the azimuthal, as expected from the linear eigenfunction of the dominant COS mode (and indeed any epicycle). The second thing is that the vertical kinetic energy is out of phase with the horizontal. We associate the vertical energy with the higher order inertial waves that attack the primary mode via the parametric instability. As a consequence, we interpret the long-time oscillations as a gentle predator–prey cycle: once the COS mode has attained a sufficiently large amplitude its energy is redistributed to the parasitic modes, which grow and peak shortly afterwards; next, with their source of energy diminished, the parasites' amplitudes decrease because of viscosity, letting the dominant COS rise again. Similar, albeit more violent, predator–prey dynamics characterizes the MRI when near criticality (Lesaffre et al. 2009).

To directly verify that the cycles are controlled by the three-wave parametric coupling, in Fig. 4 we plot the time-evolution of the filtered amplitudes of the strongest modes. These are labelled by their horizontal and vertical wavenumbers $(k_x,\ k_z)$ in units of $2\pi/L$. Rather than plot the power in a given velocity component, we employ the horizontal epicyclic speed $u_A = \sqrt{u_x^2 + 4(u_y')^2}$ because it screens out the fast oscillations of the primary mode, and partially smooths out the time-series of other modes.

Fig. 4 shows that by far the most energy lies in the leading COS mode (0,1). Next are the modes (2.5,1) and (2.5,2) which possess comparable energies that track each other in time: these are the two parasitic inertial waves in three-wave resonance with the primary. Theory predicts their wavenumbers are $k_x = 2.49$ and $k_z = 1,\ 2$, which cements the identification (L16), and also indicates there

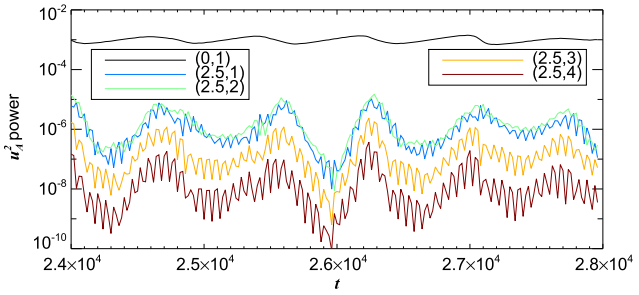

Figure 4. Largest spectral components of u_A as a function of time. Simulation parameters are $R = 10^{-1.5}$, Pe=$4\pi^2$, Re=$10^{3.75}$.

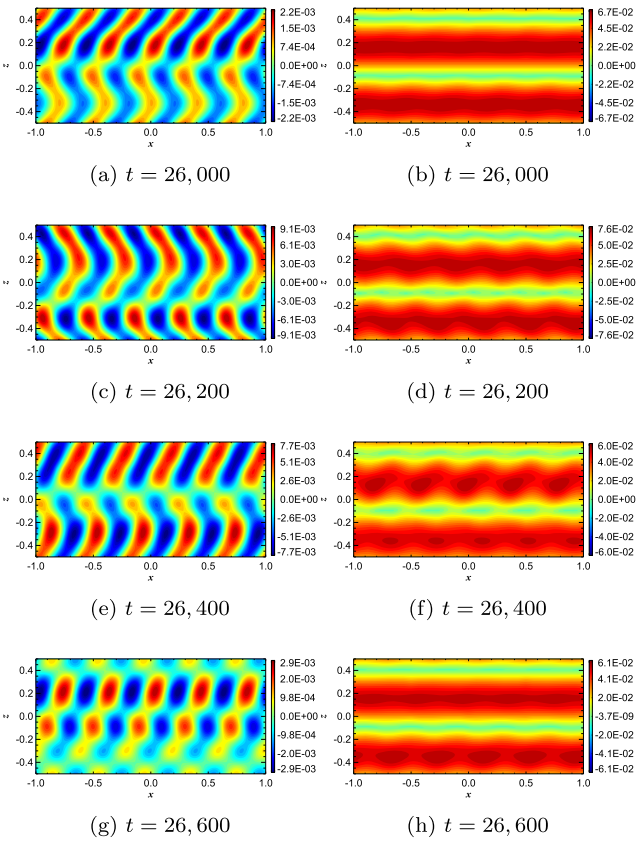

Figure 5. Plots of u_z (left-hand column) and u_A (right-hand columns) in x-z space at three times for a run saturating as the weakly non-linear regime. Simulation parameters are $R = 10^{-1.5}$, Pe=$4\pi^2$, Re=$10^{3.75}$.

is only minor detuning. In addition, there are higher order modes indicative of higher order couplings.

In Fig. 5 we show snapshots of the flow field at four different times, sampling a portion of a cycle. The vertical velocity and the horizontal epicyclic speed u_A are plotted. The flow is relatively ordered, with the horizontal motion dominated by the primary COS mode structure, though at certain times one can discern shorter scale radial features associated with the resonant modes. The vertical velocity better represents these two modes, and we can see the clear signature of their slanted spatial structures.

It is possible to construct a reduced model that can adequately describe this regime by deriving coupled evolutionary equations for the complex amplitudes of the three most dominant modes: the COS

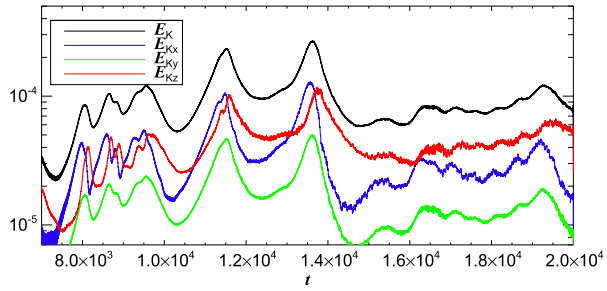

Figure 6. Kinetic energies as a function of time in a regime displaying non-linear waves and turbulence. The time series are filtered so that frequencies larger than 0.1 are removed. Simulation parameters are $R = 0.01$, Pe=$4\pi^2$, Re=$10^{5.25}$.

(labelled 'A') and the two parasitic inertial waves (labelled 'B' and 'C'). This we undertake in Appendix A, with the final reduced system given by equations (A12)–(A13). Illustrative limit cycle solutions can be reproduced that match qualitatively the behaviour shown in this section (middle panels of Fig. A2), though the cycles exhibited by the simulations are less extreme, possibly because of the participation of additional modes. One interesting prediction of the reduced model is that when sufficiently detuned the oscillations converge on to a stable fixed point and the long-time cycles disappear (left-hand panels of Fig. A1). To check this, we ran simulations in a small box with $L_x = L$ thus limiting the radial wavenumber of the two parasitic modes to $k_x = 2$, and thus relatively distant to the required 2.49. The simulated system indeed settled on a state exhibiting no long time dynamics.

5.2 Wave turbulence

On either increasing the Reynolds or pseudo-Richardson numbers (Re or R), the relatively well-ordered weakly non-linear state is replaced by a more chaotic and richer flow field in which more modes participate. This state we term wave turbulence, as it consists of many interacting inertial waves (see e.g. Nazarenko 2011), the longest driven by the COS while the others redistributing that energy to small scales.

We discuss a representative run with parameters: $R = 10^{-2}$, Pe = $4\pi^2$, and Re = $10^{5.25} \approx 1.78 \times 10^5$. For these parameters the COS driving is localized to large scales, and occurs on a range between $\lambda_{\max} = L$ and $\lambda_{\rm crit} \approx (\mathrm{Pr}/R)^{1/4} L \approx 0.35L$. An estimate for the viscous scale is $\sim \ell_{\rm visc} \sim \mathrm{Pr}^{1/2}\lambda_{\rm crit} \sim 0.01L$, and so a hint of an inertial range is possible.

In Fig. 6, we plot the time evolution of various components of the filtered kinetic energy after initial saturation. The system exhibits variability on long time-scales $\sim 1000\Omega^{-1}$ (similar to the linear COS growth time for these parameters) but, in contrast to the previous subsection, the variation is irregular and exhibits additional frequencies. Nonetheless the total kinetic energy remains $\sim R^2 \sim 10^{-4}$, in agreement with the L16 'parasitic theory' of saturation.

In Fig. 7, we plot the velocity components and θ at two different times. The velocity maps display considerably more disorder than in the weakly non-linear case, but the signatures of various slanted inertial wave-fronts emerge aperiodically. In contrast, the θ field is rather structured and its variation large scale. This is because the Peclet number is low, and the θ dynamics are dominated by strong thermal diffusion: any small-scale structures in θ generated by the velocities are wiped away rapidly. The θ spectrum is hence monoscale and is slaved to the dominant COS mode(s), which in these plots is the $k_x = 1/2$, $k_z = 1$ mode.

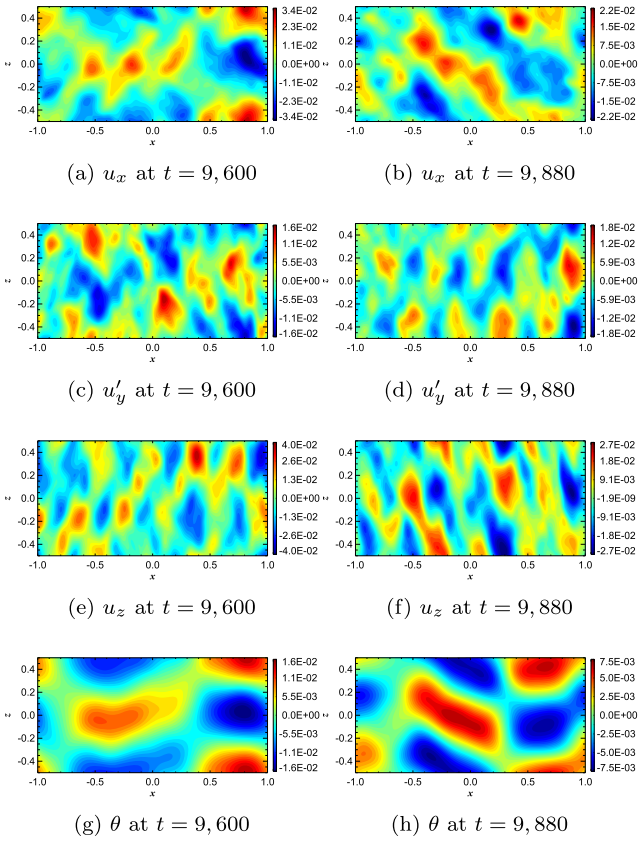

(a) u_x at $t = 9,600$ (b) u_x at $t = 9,880$

(c) u'_y at $t = 9,600$ (d) u'_y at $t = 9,880$

(e) u_z at $t = 9,600$ (f) u_z at $t = 9,880$

(g) θ at $t = 9,600$ (h) θ at $t = 9,880$

Figure 7. Plots of u_x, u'_y, u_z, and θ in x-z space at two times for a run showing wave turbulence. Simulation parameters are $R = 0.01$, Pe=$4\pi^2$, Re=$10^{5.25}$.

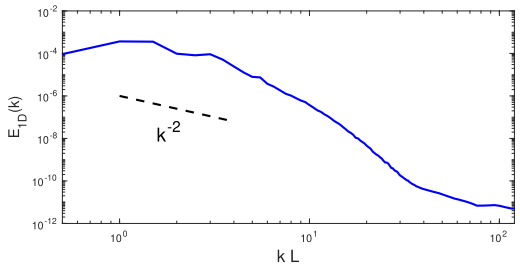

Figure 8. Power spectrum of kinetic energy as a function of wavenumber, $k = \sqrt{k_x^2 + k_z^2}$ in the wave turbulent regime. Simulation parameters are $R = 0.01$, Pe=$4\pi^2$, Re=$10^{5.25}$.

To make contact with the theory of wave turbulence we plot the 1D kinetic energy spectrum in Fig. 8. The system is not especially anisotropic, so this is sufficient for our purposes. We also superimpose the k^{-2} scaling predicted by a Kuznetsov-Zharakov turbulence theory (Galtier 2003, Nazarenko and Schekochihin 2011). As the plot shows, our simulation spectrum does not really follow a straightforward power law, probably on account of too narrow an inertial range (if one exists at all): the viscous scale is close to the input scale and thus steepens the spectrum from what it would be otherwise. As we show in Section 5.4, going to higher Re does not solve the problem, because at higher Re the system begins to develop coherent structure rather than pure wave turbulence.

Finally, though not apparent in the representative case given, wave turbulent states of larger Re and R can generate elevator flows. These

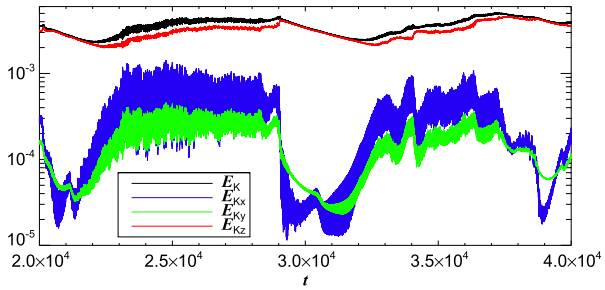

Figure 9. Kinetic energies as a function of time in a regime that fluctuates between wave turbulence and zonal flows. Simulation parameters are $R = 0.01$, Pe=$4\pi^2$, Re=$10^{5.5}$.

correspond to quasi-steady vertically homogeneous jets in u_z, and are exact solutions to our governing equations. Generally these are superimposed on the field of inertial waves and are probably excited by their non-linear mode couplings, though the details of that process is yet to be determined. Elevator flows are discussed further in the next subsection.

5.3 Zonal flows

As we increase R and/or Re, zonal flows emerge from the wave turbulence, first intermittently, and then persistently at larger values of the parameters. A zonal flow is understood here to consist of a sequence of radially varying (but vertically homogeneous) bands in u'_y and P, where the leading order force balance is between the radial pressure gradient and the Coriolis force ('geostrophic balance'). In the accretion disc context, these flows consist of a radial sequence of super-Keplerian and sub-Keplerian motion, and are exact steady solutions of our governing equations. Their excitation has been briefly discussed in Section 2.3 and we will take this up again in Section 6.

5.3.1 Intermittent flows

Initially the zonal flows emerge periodically from the inertial wave-turbulence in bursts that significantly impede the workings of that turbulence. The period of these bursts can be as long as $10^4\ \Omega^{-1}$. In Fig. 9, we plot the filtered energies as a function of time showing two long periods of wave turbulence interrupted by three shorter bursts of zonal flows, in which the kinetic energies actually drop, including the azimuthal kinetic energy. But note that during a turbulent episode $E_{Ky} < E_{Kx}$, while during a zonal-flow episode $E_{Ky} \gtrsim E_{Kx}$. It is also worth pointing out that elevator flows persist throughout, and in fact dominate the kinetic energy budget.

The velocity components are plotted in Fig. 10 at two times, the first during a zonal-flow burst, and the second during wave turbulence. In the former case, the system exhibits considerable order and a clear signature of zonal flows in u'_y (the vertically homogeneous bands). The elevator flows appear in u_z, also as vertically homogeneous bands.

The emergence and collapse of zonal flows from inertial wave turbulence has been witnessed in local simulations of eccentric discs by Wienkers and Ogilvie (2018), who model the phenomena in detail with a predator–prey style of dynamical system.[4] Something similar

[4]Models of planetary interiors or atmospheres also develop similar cycles, termed 'bursts of convection' (e.g. Teed et al., 2012).

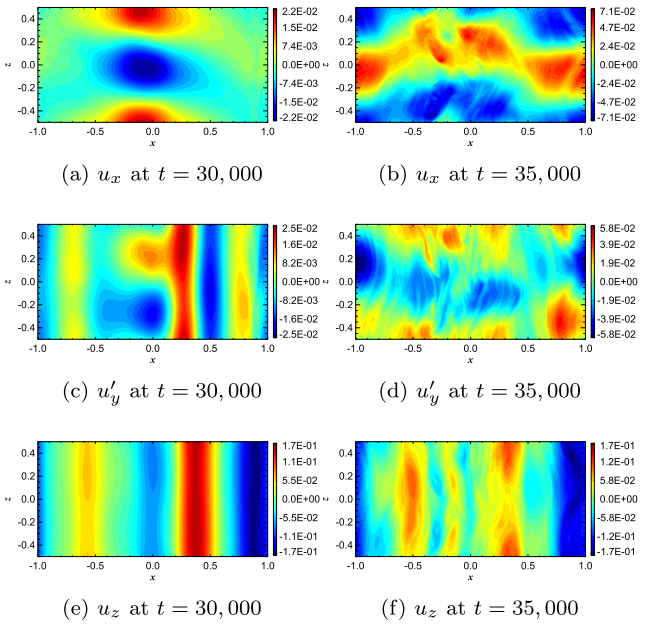

(a) u_x at $t = 30,000$ (b) u_x at $t = 35,000$

(c) u'_y at $t = 30,000$ (d) u'_y at $t = 35,000$

(e) u_z at $t = 30,000$ (f) u_z at $t = 35,000$

Figure 10. Plots of u_x, u'_y, and u_z in x-z space at two times for a run exhibiting intermittent zonal flows (left-hand panels) that emerge from periods of pure wave turbulence (right-hand panels). Simulation parameters are $R = 0.01$, Pe=$4\pi^2$, Re=$10^{5.5}$.

appears to be going on in our simulations, though we only sketch out the main features. The basic cycle consists of (i) the growth of a zonal flow out of the sea of inertial waves driven by the COS (discussed in Section 6), which (ii) acts to scatter/impede the leading COS modes, and thus reduce the input of energy from the thermal gradient, and hence the strength of the COS turbulence itself; as a result, (iii) the zonal flows are no longer excited/sustained and decay due to residual turbulent motions or viscosity, and (iv) the leading COS modes are free to grow once more and instigate inertial wave turbulence, allowing the cycle to repeat. The key difference to eccentric disc simulations is that our zonal flows degrade the primary oscillation (the dominant COS mode) rather than detune the parametric resonance attacking the primary (eccentric) oscillation (which is fixed in the simulations of Wienkers and Ogilvie).

5.3.2 *Persistent flows*

As R and/or Re increase further the zonal flows become stronger and the periods of wave turbulence shorter. Ultimately we pass through a bifurcation and the system achieves a state characterized by a quasi-steady balance between the excitation and degradation of the leading COS mode(s) and of the zonal flow. The time evolution of the energies is plotted for a fiducial example in Fig. 11, where now clearly the azimuthal kinetic energy dominates the radial kinetic energy. The latter, however, is not zero and provides evidence of COS activity working away in the background to sustain this state.

In addition, we plot the velocity components and pressure in Fig. 12 at two different times to indicate the relatively ordered configuration achieved, at least in the dominant y and z velocities. Interestingly, the weaker x-component of the velocity tends to localize in certain radial regions: the zonal flow appears to push this inertial wave activity into narrow bands, though it cannot be fully suppressed or else the zonal flows themselves would decay to zero. Similar dynamics is witnessed in semiconvection and the zonal

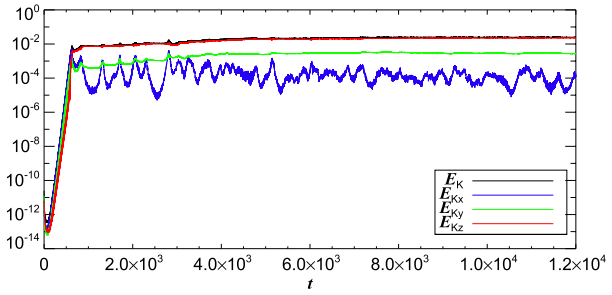

Figure 11. Kinetic energies as a function of time in a regime containing strong, persistent zonal flows. Simulation parameters are $R = 0.1$, Pe=$4\pi^2$, Re=$10^{5.5}$.

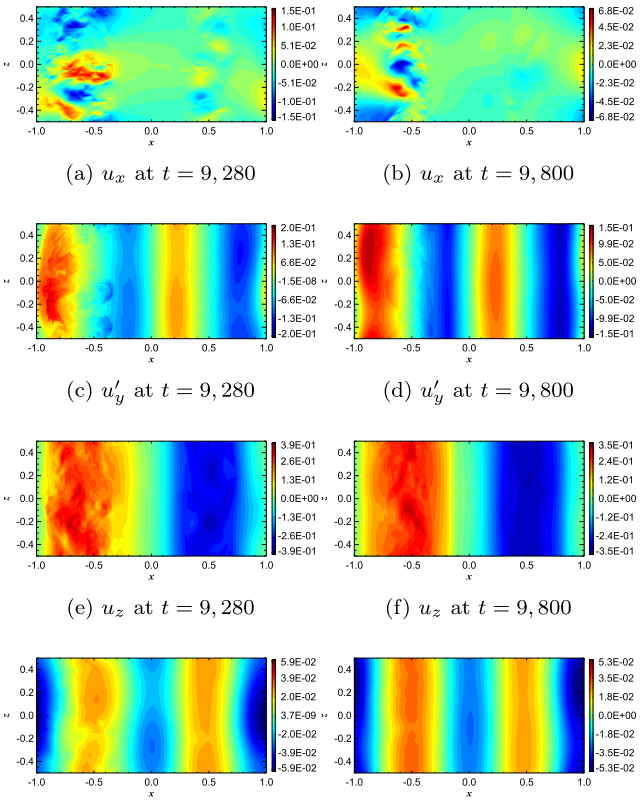

(a) u_x at $t = 9,280$ (b) u_x at $t = 9,800$

(c) u'_y at $t = 9,280$ (d) u'_y at $t = 9,800$

(e) u_z at $t = 9,280$ (f) u_z at $t = 9,800$

(g) p' at $t = 9,280$ (h) p' at $t = 9,800$

Figure 12. The perturbed velocity components and the perturbed pressure p' in x-z space at two times for a run showing persistent zonal flows. Simulation parameters are $R = 0.1$, Pe=$4\pi^2$, Re=$10^{5.5}$.

flows/fields supported by the Hall-MRI (Mirouh et al. 2012; Kunz and Lesur 2013).

The quasi-steady nature of the flows allows us to check whether they obey geostrophic balance, as claimed. We take the data from Fig. 12 at $t = 9800$, vertically average, and then plot $2u'_y$ and $\partial p/\partial x$ in Fig. 13. As is clear, the two fields lie over each other almost perfectly, verifying that geostrophic balance holds to a very high level of approximation and that these are indeed zonal flows.

The ordered flows exhibit a characteristic radial wavelength that increases over time as the flows gradually merge or disappear. This 'inverse cascade' halts once a characteristic length scale is achieved; in our $2L \times L$ boxes this length scale equals the vertical length scale of the fastest growing COS mode $2\pi\sqrt{\xi/\Omega}$. But for our choice of

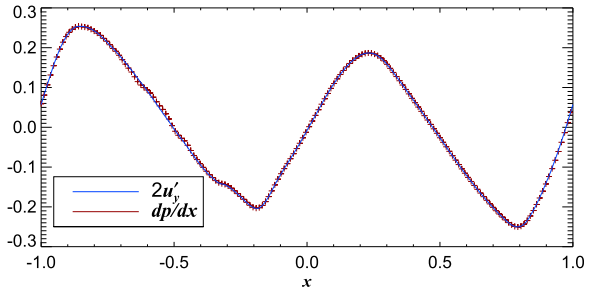

Figure 13. u'_y and dp/dx averaged over z at $t = 9800$ (corresponding to the snapshots seen in panels 12d and 12h). Simulation parameters are $R = 0.1$, Pe=$4\pi^2$, Re=$10^{5.5}$.

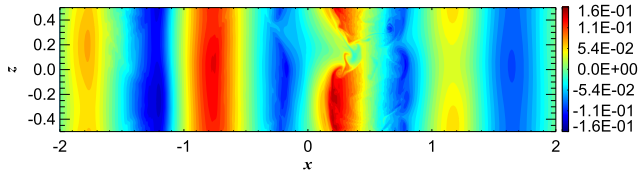

Figure 14. Plot of u'_y in x-z space for a run with $L_x = 4L_z$ that displays persistent zonal flows in its saturated state. Simulation parameters are $R = 0.1$, Pe=$4\pi^2$, Re=2×10^5.

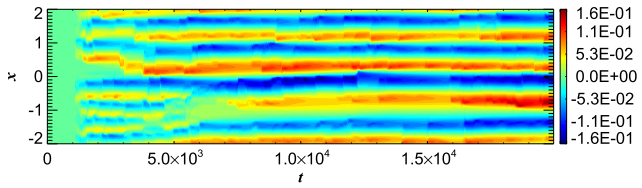

Figure 15. Space-time plot of u'_y, averaged over y and z, in t-x showing the evolution of persistent zonal flows. Simulation parameters are $R = 0.1$, Pe=$4\pi^2$, Re=2×10^5 with $L_x = 4L_z$.

Pe, it also happens to be equal to the vertical box size and half the horizontal box size. As a consequence, one might conclude that the inverse cascade is only halted by the box, and would otherwise continue indefinitely (as in staircase formation in semiconvection; e.g. Rosenblum et al. 2011; Mirouh et al. 2012; Zaussinger and Spruit 2013). To check this, we ran a simulation with double the horizontal box size, and show these results in Figs 14 and 15. The latter space–time plot demonstrates the merging of zonal flows between $t = 0$ and $t = 5 \times 10^3$, but also shows that the process stalls from that point on. For the rest of the simulation, the system is in a 'glassy' state, with the same wavelength as in the smaller box. This simulation provides some evidence that there is a well-defined characteristic scale of variation that the zonal flows converge towards.

5.3.3 Secondary instability

We now discuss the possibility that the elevator and zonal flows are subject to secondary shear instability that could break them up and/or form vortices. We consider the elevator flows first.

As the vertical velocity exhibits considerable x-periodic shear we might expect a form of Kelvin–Helmholtz instability (KHI) via the inflection point theorem. If the elevator flows have a radial wavelength of $\lambda_{\rm el}$, then quite generally the instability grows on vertical wavelengths longer than this. Given that $\lambda_{\rm el} = L_z$, one might assume that the KHI modes may not fit into our numerical domain. However, this fails to account for the stabilizing influence of rotation, which imparts an 'elasticity' to the shear flow that resists its deformation. Instability only occurs for sufficiently strong velocities and/or gradients: $V_z \gtrsim \lambda_{\rm el}\Omega$, where V_z is the maximum elevator flow amplitude (Latter and Papaloizou 2018). Our simulations never support vertical flows this strong, and thus we do not expect KHI even in larger boxes. We conclude that elevator flows are a robust and unavoidable by-product of the COS in local models.

Zonal flows, on the other hand, are subject to non-axisymmetric instability and encounter no equivalent resistance from the rotation. Generally, if the flow exhibits an extremum in the potential vorticity (or a related quantity), shear instability sets in (Papaloizou and Pringle 1985; Papaloizou and Lin 1989; Papaloizou and Savonije 1991; Lovelace et al. 1999). Often it is called 'Rossby wave instability', though the link to actual Rossby waves is somewhat tenuous. In any case, our x-periodic lattice is surely unstable to non-axisymmetric modes that will generate vortices once they reach sufficient amplitudes. Of course, being axisymmetric our simulations are unable to capture this shear instability. But in a fully 3D set-up we anticipate the zonal flow regime to naturally produce non-axisymmetric structure (as witnessed in previous work; Lyra 2014; Raettig et al. 2021). In fact, we expect that it is precisely via shear instability that the COS can break its inherent axisymmetry and give rise to disordered 3D flow, in particular vortices (which may then be sustained against instability via the subcritical baroclinic instability perhaps; Lesur and Papaloizou 2010). Future simulations will confirm this.

5.4 Parameter survey

5.4.1 Regimes

In this subsection, we vary both R and Re and plot out the boundaries between the various saturation outcomes in this 2D parameter space. The demarcation is often somewhat loose, with one state 'blurring' into the other; nonetheless, it is possible to construct a relatively reliable plot, which we show in Fig. 16. Here the green markers represent the weakly non-linear state (WNL), the blue markers represent the pure wave turbulent state (WT), the red markers indicate a regime of alternating wave turbulence and zonal flows (WTZF), and finally cyan denotes persistent zonal flows (ZF). A triangular marker indicates the presence of elevator flows. The red line is the stability boundary for the COS; regions to its left are stable.

The trend in the figure is rather clear, larger R and Re favour zonal flows. A rough boundary between pure wave turbulence and these flows (for sufficiently large Re) is given by the cyan line, $R \propto {\rm Re}^{-1/2}$ the form of which we motivate in later sections. In fact, most of the parameter space supports such flows whether they are intermittent or quasi-steady. Realistic PP discs exhibit Re $>10^7$ (according to our definition), and thus would appear to support the steady zonal flow regime unless the thermal driving R is very low. But if R is much less than 0.01 the time-scales of the COS become unfeasibly long, and the COS irrelevant. It follows that if the COS features in PP disc dynamics it will always generate zonal flows.

5.4.2 Fluxes and energies

Associated with the various states is the transport of angular momentum and heat. It is important to note that, while inviscid axisymmetric

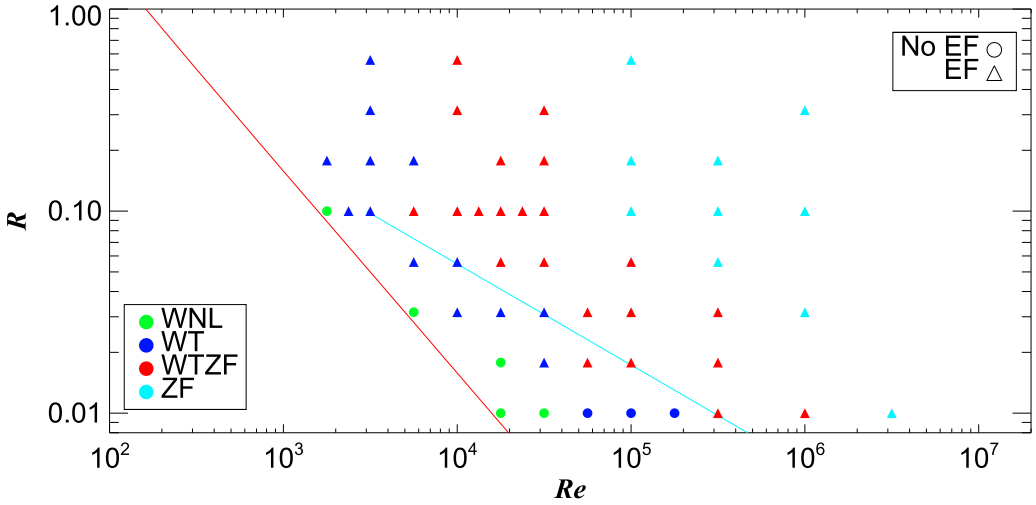

Figure 16. Plot depicting the different saturation routes open to the system in Re-R space. The red line indicates marginal COS stability (when $\lambda_{\rm crit} = L$). The cyan line loosely denotes the boundary between pure wave turbulence and zonal flows and is given by $R = 0.05 \times (\mathrm{Re}/10^4)^{-1/2}$.

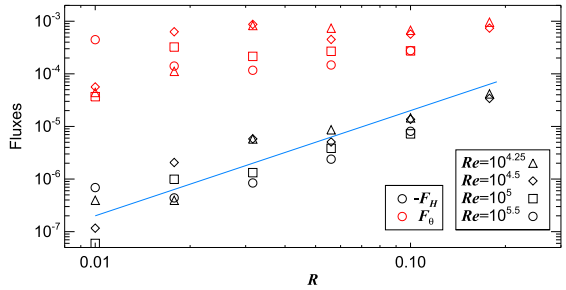

Figure 17. Turbulent fluxes, $F_H = \langle u_x u_y' \rangle$ and $F_\theta = \langle u_x \theta \rangle$, as functions of R for Pe=$4\pi^2$. The blue fitting line is given by $2 \times 10^{-7}(R/0.01)^2$.

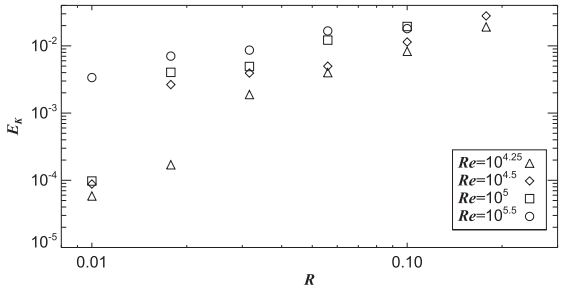

Figure 18. Kinetic energy averaged in space and time (during saturated state) as a function of R for Pe=$4\pi^2$, for selected simulations.

inertial waves are unable to carry angular momentum, unstable COS modes can in fact produce a small flux on account of the small modification to their period by buoyancy accelerations (see fig. 2 in L16). From linear theory we find that the flux of angular momentum is

$$F_H = 2\mathrm{Re}[u_x'(u_y')^*] \approx -|u_x'|^2(\mathrm{Re}(s)/\Omega), \quad (9)$$

where u_x' and u_y' are the linear velocity perturbations, and s is the real part of the COS growth rate for that particular mode. As is clear the flux is non-zero and negative.

We plot the mean thermal and angular momentum fluxes, F_θ and F_H in Fig. 17. The angular momentum flux remains small and negative, and apart from its role in causing the emergence of zonal flows (cf. Section 6), its impact on the large-scale evolution of the disc should be minimal. The thermal flux is outward and is much larger. It acts to equalize the unstable gradient that gave rise to the COS, and takes values, in our units, as high as $\sim 10^{-3}$. However, it is never on par with the radiative diffusive flux, which may be estimated to be $\sim \mathrm{Pe}^{-1} \sim 2.5 \times 10^{-2}$ (for an order one background variation in entropy varying on the box scale). Both fluxes increase in magnitude with R, as the system moves through the different states. Putting to one side variations associated with these transitions, the angular momentum flux appears to follow the rough scaling $F_H = -2 \times 10^{-7}\,(R\,/\,0.01)^2$, in our units.

For completeness we plot the kinetic energies in Fig. 18. As the thermal driving increases so does the energy, though this is more pronounced at lower Re, mainly because these runs exhibit more state transitions. The WNL and WT states possess significantly weaker energies than those states that exhibit elevator and zonal flows. Velocities in the latter states can be an order of magnitude or larger, and thus easily violate the estimate in equation (35) in L16 derived from the 'parasitic' theory of saturation. Finally, we point out that the jumps in energy as one progresses to these ordered 'layered' states is also a notable feature in semiconvection.

6 PHYSICAL MODEL FOR LAYER FORMATION

In this section, we expound a physically intuitive theory for why zonal flows might develop in COS turbulence. It is well established that 3D rotating turbulence manifests large-scale coherent structures via an inverse cascade (e.g. Cambon and Jacquin 1989, Mininni et al. 2009), but our simulations are not 3D, and the details of the nonlinear transfer amongst the wave modes are difficult to unpick (but see Smith and Waleffe, 1999; Kerswell 1999; Le Reun et al. 2020). Here, we sketch out some principles and arguments that help us with our physical intuition. These ideas are fleshed out with a mean field model similar in spirit to Radko (2003), Rosenblum et al. (2011), and Mirouh et al. (2012), the details of which we package away in Appendix B. The predictions of this model we confront with our numerical simulations at the end of the section.

6.1 Basic principles: competing gradients and fluxes

Ours is a story of two opposed gradients. There is an outwardly decreasing entropy gradient ($N^2 < 0$), which is destabilizing, and an outwardly increasing angular momentum gradient ($\kappa^2 > 0$), which is stabilizing. The COS uses thermal diffusion to circumvent the angular momentum gradient in order to grow, and yet it is still sensitive to κ^2 because its (maximum) growth rate is proportional to the ratio $-N^2/\kappa^2 = R$. While, it is clear that a larger $|N|$ exacerbates instability (because the entropy gradient is the source of free energy), interestingly a steeper angular momentum gradient (larger κ^2) inhibits instability, and conversely, a flatter gradient (smaller κ^2) enhances it.[5] In fact, in the limit of a constant angular momentum disc ($\kappa = 0$), the COS ceases to be an overstability, as epicycles and inertial waves vanish; we then obtain standard convection growing at the significantly larger rate of $|N|$ (albeit modified by the thermal diffusion). In summary, the angular momentum gradient, while not precluding instability, does get in the way; it obliges unstable modes to undergo oscillatory motion, which are unnecessary to the transport of heat. If these superfluous motions are minimized, instability works better.

These concepts can be extended beyond linear theory if we consider how the ensuing turbulence transports both θ and angular momentum locally. By virtue of this transport, small but significant variations in the local distribution of both entropy and angular momentum can develop. These variations can then feedback on the driving of the instability in the non-linear regime.

As we have seen in Section 5.4.2, and in Fig. 17, the turbulent heat flux generated by the COS is outward, and thus augments (slightly) the laminar diffusive flux. This is as expected: the COS is trying to eliminate the unstable state from which it arose; by mixing entropy, $|N|$ can be reduced. If we define an effective radially and temporally varying R, then locally this R will decrease and the linear driving will weaken.

But we also observe a small inward transport of angular momentum. Because angular momentum increases outward, the turbulence works to flatten this gradient: thus reducing κ^2. Consequently, the locally varying R will increase in magnitude. This transport, though weak, exacerbates instability (the COS growth rate is $\propto |N^2|/\kappa$). Though not a strong effect in relative terms, we shall find it is critically important for the local distribution of angular momentum – and may lead to antidiffusion.

6.2 An antidiffusive angular momentum flux

Let us work through the consequences of these basic ideas in a wave turbulent state. Suppose that this turbulent state supports an inward turbulent flux of angular momentum $F = -\langle u_x u'_y \rangle$, with $F > 0$, and that viscous diffusion may be ignored for the moment. Let us assume, reasonably, that this flux F depends locally on the strength of the COS turbulence at that location: the stronger the turbulence the more transport takes place. Next, suppose that this turbulent strength is an increasing function of the local R parameter: thus we may write $F = F(R)$, and $\mathrm{d}F/\mathrm{d}R > 0$. (Fig. 17 certainly helps justify these statements.) Finally, let us define the local effective R parameter as a ratio of the total entropy gradient and the total angular momentum gradient:

$$R_{\rm eff} = \frac{N^2 \partial_x \theta_x}{2\Omega \partial_x h}, \tag{10}$$

which returns to the constant $R = -N^2/\kappa^2$ in the unperturbed state. The local COS intensity will be tuned to the magnitude of this locally varying R.

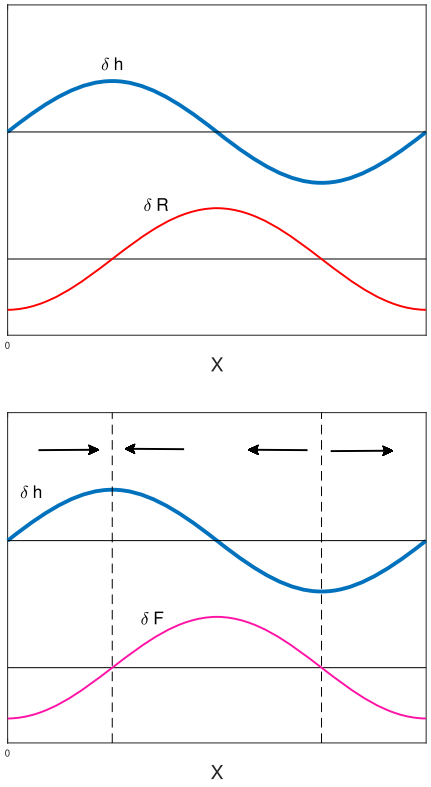

Figure 19. Sketch of how zonal flows may develop in COS turbulence. See the text for an explanation.

Suppose there is a large-scale sinusoidal x-dependent perturbation to the background angular momentum $h_0(x)$. We call it δh and plot it in the top panel of Fig. 19. Because of the sinusoidal shape of δh, the total angular momentum gradient is slightly flatter in the middle of the box, and slightly steeper at the edges of the box. As a consequence of this flattening and sharpening, the disturbance drives a perturbation in the local $R_{\rm eff}$ parameter, which we denote by δR. It will be $\pi/2$ out of phase with δh. Next, if the turbulent intensity, and hence any turbulent flux, depends on $R_{\rm eff}$, the perturbation in the inward flux of angular momentum, denoted δF will be correlated with δR, as shown in the bottom panel of Fig. 19. Now radial regions in which δF is positive experience an additional momentum flux, and where it is negative a smaller momentum flux: the arrows in the bottom panel indicate the direction of the perturbed flux (note that the total flux will be inward for all x). As is clear, this means that peaks of δh will increase, and troughs decrease, leading to a runaway process, and the development of radial layers of angular momentum: i.e. zonal flows.

Working against this tendency is viscous diffusion, which, given the weakness of the angular momentum flux, is not necessarily negligible. Hence any criterion of zonal formation must tension the perturbed turbulent angular momentum flux against the perturbed viscous flux. If we neglect buoyancy perturbations, the former can be written as $-(\mathrm{d}F/\mathrm{d}R)\delta R = 2(\Omega/\kappa^2)(R\mathrm{d}F/\mathrm{d}R)(\partial_x \delta h)$, while the latter

[5]This point could be rephrased in terms of 'wave elasticity'. See Dritschel and McIntyre (2008)

is $-\nu\partial_x\delta h$. Clearly, the turbulent flux overpowers the viscous flux when

$$\frac{\mathrm{d}F}{\mathrm{d}\ln R} > \frac{\kappa^2\nu}{2\Omega}, \tag{11}$$

which is our criterion for zonal flow formation. In principle, accompanying variations in the turbulent flux of entropy works against this antidiffusion and should also enter the criterion, but the effect is small when the laminar radiative flux dominates the turbulent flux, as is the case in our simulations. In Appendix B, we construct a mean field model that accounts for this additional physics, and puts some of the ideas in this section on a more mathematical footing. (In the notation of Appendix B, $F = -F_H$.)

6.3 Comparison with simulations

We next apply criterion (11), a posteriori, to our simulation data, though we must heed some caveats. Perhaps the greatest issue is that our arguments have relied on a separation of scales that the simulations do not generally exhibit. Is there enough space in our simulation domain for a mean flux to be defined as we have done, when the eddies are only a bit smaller than the box size? Moreover, can R exhibit meaningful variations on scales so close to the characteristic turbulent length scales, and thus provide the associated x-dependent COS driving? Though it is difficult to answer these questions in the affirmative, our mean field model can capture in some sense the underlying physics taking place, and as we shall see is roughly consistent with the results.

In our code units the criterion can be reframed as $\mathrm{d}F/\mathrm{dln}\,R > (1/2)\mathrm{Re}^{-1}$. We may then use our numerically determined scaling for F, obtained in Section 5.4.2: $F \approx 2 \times 10^{-7}(R/0.01)^2$, which holds within the regime of weak turbulence (but not outside). The revised zonal flow criterion becomes simply $R \gtrsim 0.1(\mathrm{Re}/10^4)^{-1/2}$. This should be compared to the cyan line in Fig. 16, which is given by $R = 0.05\,(\mathrm{Re}/10^4)^{-1/2}$. The two curves differ by an order one factor, which (given the many approximation involved) is not too bad. (At lower Re it appears that the system is just too viscous for the theory to be applicable.) In summary, the comparison does seem to justify the mean field theory, and most importantly provides support for our physical explanation of zonal flow formation.

7 CONCLUSION

In this paper, we have explored the non-linear development of the convective overstability (COS) in a local model of a protoplanetary disc. Our main aim has been to categorize and determine the underlying physics of the several dynamical regimes the instability supports. Of particular interest is the onset of the coherent structures known as zonal flows, which comprise a radial sequence of vertically homogeneous azimuthal jets. They are important because they provide a route by which the COS can break its inherent axisymmetry (via a non-axisymmetric shear instability) and thence develop fully 3D flow, vortices most importantly. Though our simulations are axisymmetric, and thus cannot describe vortex production, what they can do is establish the critical parameters required to obtain zonal flows; and being only 2D we can push our parameters to values nearly representative of real PP discs.

The non-linear dynamics of the COS, even in axisymmetry, is remarkably rich. Our main parameters are the Reynolds number Re and a number describing the unstable entropy gradient R (which we sometimes call the 'pseudo-Richardson number'). For values of Re and R near criticality, the system supports interesting non-linear waves, which involve a three-way resonance linking the primary COS mode and two daughter inertial waves (cf. Section 5.1). The principle features of this state can be captured analytically by a weakly non-linear analysis (Appendix A). As we push Re and R to larger values away from criticality, the system enters a more disordered state that shares some features with inertial wave turbulence (Galtier 2003), though its inertial range is too short to make more than passing contact with weak turbulence theory (cf. Section 5.2). We expect the non-linear wave and wave turbulent states to remain axisymmetric even when simulated in full three dimensions.

On increasing either or both Re and R further, zonal flows begin to emerge intermittently and enter a predator–prey cycle with the wave turbulence. The latter, when sufficiently strong, drives the growth of the coherent structures but is then impeded by them, leading to oscillatory dynamics (cf. Section 5.3). For larger Re and/or R the zonal flows become persistent and the COS turbulence and the coherent structures agree on a quasi-steady state. Concurrently, the system exhibits elevator flows, which consist of a radial pattern of upward and downward velocities; they appear to be forced by inertial wave turbulence through a process yet to be understood. Elevator flows are robust features in local models of discs because the Kelvin-Helmholtz instabilities that might otherwise break them down are suppressed by rotation. The development of zonal flows, on the other hand, is a generic feature of any rotating flow, and similar features appear in semi-convection, which shares many mathematical and physical details (e.g. Cambon and Joaquin 1989, Smith and Waleffe 1999, Mirouh et al. 2012). We construct a mean-field theory in Section 6 and Appendix B that illuminates some of the underlying physics behind their onset in COS unstable discs. But how zonal flows saturate, be it through a cyclical predator–prey dynamics with inertial wave turbulence or a steady balance with the same, is not entirely clear to us and forms the basis of future work.

Astrophysically, the most important boundary in the parameter space is that separating the wave-turbulent state from the intermittent zonal-flow state, as the latter is a possible site of vortex production. According to our simulations, this boundary curve can be fitted by $R = 0.05 \times (\mathrm{Re}/10^4)^{-1/2}$ (cf. Section 5.4). In realistic PP discs, Re takes values $\sim 10^7$ at 1 AU to $\sim 10^{10}$ at 10 AU (using our definition of Re; Section 3.2), which means that zonal flows only fail to appear when R is smaller than $R_{\mathrm{crit}} \sim 10^{-3}$ (1 AU) or 10^{-4} (10 AU). As discussed in Section 2.2, it is difficult to determine what values R realistically adopt; but what can be said is that the characteristic time-scale of the COS is $\sim R^{-1}\Omega^{-1}$ and thus when $R < R_{\mathrm{crit}}$ the COS is certainly operating too slowly at 10 AU to play a role in the disc dynamics, and is on the sluggish side at 1 AU. We conclude that if the COS is functioning on a reasonable time-scale in PP discs it will probably be in the regime of zonal flows and hence of potential vortex formation.

The COS, being small-scale, will generate vortices that will also be small-scale, initially with lengths $\sim \sqrt{\xi/\Omega}$, and hence not observable. Even if small, vortices can collect solids and actively take part in planet formation, and while they will certainly be subject to secondary instability (Lesur and Papaloizou 2009; Railton and Papaloizou 2014), they may also be protected from complete dissolution by the subcritical baroclinic instability mechanism once they have formed (Lesur and Papaloizou 2010).

As with any project of numerical simulation, compromises have had to be made. We adopted the diffusion approximation for radiative cooling, which may not be suitable at larger radii and for less massive discs. Though some of the fine details may need revision, we believe that our picture of zonal flow production should carry across. Our simulations are also local and ideally we would want a separation of scales between the box size and the energy input size (and indeed

any larger scale structure that might develop), and also between the energy input size and the viscous length. Given our resources, we cannot achieve both at the same time and so have chosen to explore the latter separation of scales, thus allowing us the chance to simulate discs approaching realistic molecular viscosities at the inner radii of PP discs, a novelty that we could not resist. This choice does mean that the large-scale coherent structures that develop in our simulations (zonal and elevator flows) are possibly impacted upon by the numerical box. Additional simulations might explore the opposite regime, where the box is much larger than the COS input scale, so as to check that box-size effects are not critical to what we show here (cf. convergence issues in Lyra 2014). Different vertical boundary conditions could also be trialled, such as impermeable walls (e.g. Barker et al. 2019).

Future work includes 3D simulations to observe how zonal flows wrap up into vortices, and whether this is possible in the intermittent zonal flow regime. Such a numerical program can also determine how these vortices self-sustain once formed (using the background entropy gradient), how large they get, how long they live, etc. Forthcoming studies might explore the influence of important physical processes omitted so far. While a stable vertical entropy gradient has no effect on the fastest growing modes, it will alter their ensuing non-linear wave resonances, and consequently the wave turbulence; its impact on the elevator flows will be even more pronounced. Similarly, vertical shear will not impede the fastest COS modes, but could modify their non-linear saturation, as might the VSI if present. Finally, the non-ideal MHD element of the problem could be assessed: not only how magnetic tension impedes instability, but how the vorticity dynamics inherent in the COS evolution combines with the Hall effect (cf. Kunz and Lesur 2013). Such a project might also explore the non-linear development of the resistive double diffusive instability (Latter et al. 2010), which is fuelled from the same energy source as the COS, and may compete with the COS under certain circumstances.

ACKNOWLEDGEMENTS

The authors thank the reviewer for a useful set of comments, and Gordon Ogilvie, Wlad Lyra, Min-Kai Lin, and Tobias Heinemann for helpful conversations and/or feedback on the manuscript. This work was partially funded by STFC grant ST/L000636/1.

DATA AVAILABILITY

The data underlying this article will be shared on reasonable request to the corresponding author.

REFERENCES

Andrews S. M., Wilner D. J., Hughes A. M., Qi C., Dullemond C. P., 2009, ApJ, 659, 705
Armitage P. J., 2011, ARA&A, 49, 195
Arras P., Flanagan E., Morsink S., 2003, ApJ, 591, 1129
Barker A. J., Jones C. A., Tobias S. M., 2019, MNRAS, 487, 1777
Brogan C. L. et al., 2015, ApJ, 808, L3
Bussac M. N., 1982a, Phys. Scr., 2, 110
Bussac M. N., 1982b, Phys. Rev. Lett., 49, 1939
Calzavarini E., Doering C. R., Gibbon J. D., Lohse D., Tanabe A., Toschi F., 2006, PhRvE, 73, 035301
Cambon C., Jacquin L., 1989, JFM, 202, 295
Chiang E., Youdin A. N., 2010, Annu. Rev. Earth Planet. Sci., 38, 493
Chrenko O., Nesvorny D., 2020, A&A, 642, 219
Craik A. D. D., 1985, Wave Interactions and Fluid Flows. Cambridge Univ. Press, Cambridge
de Gregorio-Monsalvo I. et al., 2013, A&A, 557, 133
Dewberry J. W., Latter H. N., Ogilvie G. I., Fromang S., 2020, MNRAS, 497, 435
Diamond P. H., Itoh S. -I., Itoh K., Hahm T. S., 2005, Plasma Phys. Control. Fusion, 47, 35
Dritschel D. G., McIntyre M. E., 2008, J. Atmos. Sci., 65, 885
Dullemond C. P., Dominik C., Natta A., 2001, ApJ, 560, 957
Fedele D., Carney M., Hogerheijde M. R., Walsh C., Miotello A., Klaassen P., Bruderer S., Henning Th., van Dishoeck E. F., 2017, A&A, 600, 72
Flaherty K. et al., 2017, ApJ, 843, 150
Flaherty K., Hughes M., Rosenfeld K., Andrews S., Chiang E., Simon J., Kerzner S., Wilner D., 2015, ApJ, 813, 99
Flaherty K., Hughes M., Teague R., Simon J., Andrews S., Wilner D., 2018, ApJ, 856, 117
Frisch U., 1989, in Herring J. R., McWilliams J. C., eds, Lecture Notes on Turbulence, NCAR-GTP Summer School June 1987. World Scientific, Singapore
Galtier S., 2003, Phys. Rev. E, 68, 015301
Gammie C. F., 1996, ApJ, 457, 355
Garaud P., Lin D. N. C., 2007, ApJ, 654, 606
Goldreich P., Lynden-Bell D., 1965, MNRAS, 130, 125
Greenspan H. P., 1969, JFM, 36, 257
Guilloteau S., Dutrey A., Pié tu V., Boehler Y., 2011, A&A, 529, 105
Hughes D. W., Proctor M. R. E., 1990, Phys. D, 46, 163
Hughes D. W., Proctor M. R. E., 1992, J. Fluid Mech., 244, 583
Isella A., Carpenter J. M., Sargent A. I., 2009, ApJ, 701, 1746
Jacquet E., Balbus S., Latter H., 2011, MNRAS, 415, 3591
Jankovic M. R., Owen J. E., Mohanty S., Tan J. C., 2021, MNRAS, 504, 280
Johansen A., Youdin A., Klahr H., 2009, ApJ, 697, 1269
Kerswell R. R., 1999, JFM, 382, 283
Klahr H. H., Bodenheimer P., 2003, ApJ, 582, 869
Klahr H., Hubbard A., 2014, ApJ, 788, 21
Kunz M., Lesur G., 2013, MNRAS, 434, 2295
Latter H. N., 2016, MNRAS, 455, 2608
Latter H. N., Balbus S. A., 2012, MNRAS, 424, 1977
Latter H. N., Bonart J. F., Balbus S. A., 2010, MNRAS, 405, 1831
Latter H. N., Lesaffre P., Balbus S. A., 2009, MNRAS, 394, 715
Latter H. N., Papaloizou J., 2017, MNRAS, 472, 1432
Latter H. N., Papaloizou J., 2018, MNRAS, 474, 3110
Latter H. N., Rosca R., 2017, MNRAS, 464, 1923
Le Reun T., Gallet B., Favier B., Le Bars M., 2020, JFM, 900, R2
Lecar M., Podolak M., Sasselov D., Chiang E., 2006, ApJ, 640, 1115
Lesaffre P., Balbus S. A., Latter H. N., 2009, MNRAS, 396, 779
Lesur G., Fromang S., 2019, EAS Publ. Ser., 82, 391
Lesur G., Latter H., 2016, MNRAS, 462, 4549
Lesur G., Longaretti P.-Y., 2005, A&A, 444, 25
Lesur G., Longaretti P.-Y., 2007, MNRAS, 378, 1471
Lesur G., Papaloizou J. C. B., 2009, A&A, 498, 1
Lesur G., Papaloizou J. C. B., 2010, A&A, 513, 60
Lin M.-K., Youdin A., 2015, ApJ, 811, 17
Lovelace R. V. E., Li H., Colgate S. A., Nelson A. F., 1999, ApJ, 513, 805
Lyra W., 2014, ApJ, 789, 77
Lyra W., Klahr H., 2011, A&A, 527, 138
Lyra W., Umurhan O. M., 2019, PASP, 131, 072001
Malygin M. G., Klahr H., Semenov D., Henning Th., Dullemond C. P., 2017, A&A, 605, 30
Mininni P. D., Alexakis A., Pouquet A., 2009, PhFl, 21, 015108
Mirouh G. M., Garaud P., Stellmach S., Traxler A. L., Wood T. S., 2012, ApJ, 750, 61
Mori S., Bai X.-N., Okuzumi S., 2019, ApJ, 872, 98
Moskalik P., 1985, Acta Astron., 35, 229
Muratori S., Rinaldi S., 1989, SIAM J. Appl. Math., 49, 1462
Muto T. et al., 2012, ApJ, 748, 22
Natta A., Prusti T., Neri R., Wooden D., Grinin V. P., Mannings V., 2001, A&A, 371, 186
Nazarenko S., 2011, Wave Turbulence. Springer-Verlag, Berlin

Nazarenko S., Schekochihin A., 2011, J. Fluid Mech., 677, 134
Papaloizou J. C. B., Lin D. N. C., 1989, ApJ, 344, 645
Papaloizou J. C. B., Pringle J. E., 1985, MNRAS, 213, 799
Papaloizou J. C., Savonije G. J., 1991, MNRAS, 248, 353
Perrin M. D., Schneider G., Duchene G., Pinte C., Grady C. A., Wisniewski J. P., Hines D. C., 2009, ApJ, 707, 132
Petersen M., Julien K., Stewart G., 2007, ApJ, 658, 1236
Pfeil T., Klahr H., 2019, ApJ, 871, 150
Pinte C., Dent W. R. F., Menard F., Hales A., Hill T., Cortes P., de Gregorio-Monsalvo I., 2016, ApJ, 816, 25
Radko T., 2003, J. Fluid Mech., 497, 365
Raettig N., Lyra W., Klahr H., 2021, ApJ, 913, 92
Railton A. D., Papaloizou J. C. B., 2014, MNRAS, 445, 4409
Richard S., Nelson R., Umurhan O., 2016, MNRAS, 456, 3571
Rosenblum E., Garaud P., Traxler A., Stellmach S., 2011, ApJ, 731, 66
Simon J. B., Beckwith K., Armitage P., 2012, MNRAS, 422, 2685
Smith L. M., Waleffe F., 1999, PhFl, 11, 1608
Spruit H. C., 2013, A&A, 552, 76
Srinivasan K., Young W. R., 2012, J. Atmos. Sci., 69, 1633
Steinacker A., Papaloizou J., 2002, ApJ, 571, 413
Stellmach S., Traxler A., Garaud P., Brummell N., Radko T., 2011, J. Fluid Mech., 677, 544
Tassoul J.-L., 2000, Stellar Rotation. Cambridge Univ. Press, Cambridge
Tazzari M. et al., 2017, A&A, 606, 88
Teed R. J., Jones C. A., Hollerbach R., 2012, Phys. Fluids, 24, 066604
Traxler A., Stellmach S., Garaud P., Radko T., Brummell N., 2011, J. Fluid Mech., 677, 530
Turner N. J., Fromang S., Gammie C., Klahr H., Lesur G., Wardle M., Bai X. -N., 2014, in Beuther H., Klessen R. S., Dullemond C. P., Henning T. K., eds, Protostars and Planets VI. University of Arizona Press, Tucson, p. 411
Urpin V., Brandenburg A., 1997, MNRAS, 294, 399
Vanon R., Ogilvie G. I., 2017, MNRAS, 466, 2590
Vyshkind S. I., Rabinovich M. I., 1976, Pis'ma Zh. Eksp. Teor. Fiz., 71, 557
Wersinger J. -M., Finn J. M., Ott E., 1980, Phys. Fluids, 23, 1142
Wienkers A. F., Ogilvie G. I., 2018, MNRAS, 477, 4838
Wood T. S., Garaud P., Stellmach S., 2013, ApJ, 768, 157
Wu Y., Goldreich P., 2001, ApJ, 546, 469
Zaussinger F., Spruit H. C., 2013, A&A, 554, 119

APPENDIX A: REDUCED DYNAMICAL MODEL: THREE-WAVE COUPLING

In this appendix, we derive a simple dynamical system for the three-wave interactions governing our simulations in the weakly non-linear regime. The analysis here extends that of L16 by allowing for the feedback of the instability on the primary COS mode, in addition to energy dissipation by viscosity.

A1 Asymptotic expansions

Suppose our disc is Keplerian and consider the non-linear equations for the perturbations $\mathbf{u}'$, $h' = P'/\rho$, and θ' in units so that $\Omega = 1$ and $\sqrt{\xi/\Omega} = 1$:

$$\left(\partial_t + \mathbf{u}'\cdot\nabla\right)\mathbf{u}' = -\nabla h' + (2u_y' + R\theta')\mathbf{e}_x - \tfrac{1}{2}u_x'\mathbf{e}_y + \mathrm{Pr}\nabla^2\mathbf{u}', \tag{A1}$$

$$\left(\partial_t + \mathbf{u}'\cdot\nabla\right)\theta' = u_x' + \nabla^2\theta', \qquad \nabla\cdot\mathbf{u}' = 0, \tag{A2}$$

We introduce a small parameter $0 < \epsilon \ll 1$ and consider a regime in which $\mathrm{Pr} \sim R \sim \epsilon$. Given the stability criterion of the COS, this scaling indicates that we are near criticality. As a consequence, the saturation of the instability takes place at relatively low amplitudes, of the order of ϵ. In addition, we assume that non-linear solutions evolve on a time-scale much longer than the fast orbital time; we thus introduce a slow time variable $T = \epsilon t$. Finally, we expand the perturbations in ϵ so that

$$\mathbf{u}' = \epsilon\mathbf{u}_1(\mathbf{x}, t, T) + \epsilon^2\mathbf{u}_2(\mathbf{x}, t, T) + \ldots,$$
$$h' = \epsilon h_1(\mathbf{x}, t, T) + \epsilon^2 h_2(\mathbf{x}, t, T) + \ldots,$$
$$\theta' = \epsilon\theta_1(\mathbf{x}, t, T) + \ldots, \qquad \mathrm{Pr} = p\epsilon, \qquad R = r\epsilon,$$

where p and r are order-one 'tuning' parameters, and $\mathbf{u}_i$, h_i, and θ_i must remain of the order of one. This ansatz is thrown into the non-linear equations and terms in the various orders of ϵ are collected.

A2 Structure of the solution at order ϵ

At leading order $\mathcal{O}(\epsilon)$ we obtain the linear problem governing incompressible inertial waves:

$$\partial_t\mathbf{u}_1 = -\nabla h_1 + 2u_{1y}\mathbf{e}_x - \tfrac{1}{2}u_{1x}\mathbf{e}_y, \qquad \nabla\cdot\mathbf{u}_1 = 0. \tag{A3}$$

This can be reduced to the convenient $\mathcal{L}u_{x1} = 0$, where $\mathcal{L} = \partial_t^2\nabla^2 + \partial_z^2$ is the 'inertial wave operator'. This equation admits solutions of the form $\propto \exp(\mathrm{i}k_x x + \mathrm{i}k_z z - \mathrm{i}\omega t)$, where k_x and k_z are wavenumbers and the frequency is $\omega = \pm k_z/k$, with $k^2 = k_x^2 + k_z^2$. In our simulations' periodic domain, the wavenumbers must be discretized.

There are an infinite number of wave solutions to the problem at this order and the most general solution comprises a linear combination of them all. We consider only three: the $k_x = 0$ mode associated with the COS, and two 'daughter' modes that can couple to it via a resonance. The primary (COS) mode we denote with a subscript 'A': it has a wavevector $\mathbf{k}_A = (0, 0, k_{Az})$, and frequency $\omega_A = 1$. We select the fastest growing COS mode, which means $k_{Az} = 1$ in our dimensions.

The two daughter waves are denoted by 'B' and 'C'. In order to obtain (near) resonance we must have

$$\pm\mathbf{k}_A \pm \mathbf{k}_B \pm \mathbf{k}_C = \mathbf{0}, \quad \text{and} \quad \pm\omega_A \pm \omega_B \pm \omega_C = \Delta.$$

So as to best compare with L16 in the following the signs are chosen in the order '$--+$'. Because of the finite size of the numerical domain (and the consequent discretization of the wavenumbers) it may not be possible to achieve perfect resonance, in which case there will be some degree of detuning, represented in the above by the quantity Δ. This will be assumed small, and to ease the asymptotic ordering we set $\Delta = \delta\epsilon$, where $\delta \sim 1$ is a new parameter. This frequency mismatch comes in only at higher order. In addition, we only consider vertical wavenumbers that are discrete multiples of the primary's; thus we set $k_{BZ} = n$, where n is an integer, and so $k_{Cz} = n + 1$. Lastly, we assign $\omega_B = -n/k_B$ and $\omega_C = (n + 1)/k_C$, from the dispersion relation for inertial waves.

In summary, at this order our solution is

$$\mathbf{u}_1 = \mathbf{u}_A A(T)E_A(\mathbf{x}, t) + \mathbf{u}_B B(T)E_B(\mathbf{x}, t) + \mathbf{u}_C C(T)E_C(\mathbf{x}, t) + \text{c.c.},$$

where 'c.c.' indicates the complex conjugate of the preceding, A, B, and C are complex amplitudes (to be determined), $E_A(\mathbf{x}, t) = \exp(\mathrm{i}\mathbf{k}_A\cdot\mathbf{x} - \mathrm{i}\omega_A t)$, etc., and the constant velocity vectors are given by $\mathbf{u}_A = [1, -\mathrm{i}/(2\omega_A), -k_{Ax}/k_{Az}]$, etc.

The resonance condition ensures $k_{Bx} = k_{Cx} \equiv k_x$, so we can write $\mathbf{k}_A = (0, 0, 1)$, $\mathbf{k}_B = (k_x, 0, n)$, $\mathbf{k}_C = (k_x, 0, 1 + n)$, and given that $\omega_A = 1$, we have at leading order, in small ϵ, that $\omega_C = 1 + \omega_B$, which can be expressed in the remaining parameters:

$$\frac{n}{\sqrt{k_x^2 + n^2}} + \frac{n+1}{\sqrt{k_x^2 + (n+1)^2}} = 1. \tag{A4}$$

Given a fixed n, this condition yields a distinct k_x at which exact resonance can occur. For $n = 1 - 5$, we obtain $k_x \approx 2.49, 4.26, 6.02, 7.76, 9.50$ (see L16).

An expression for h_1 is not needed, but we do require the leading order buoyancy variable θ_1 in what follows. The buoyancy equation at leading order is a forced diffusion equation: $(\partial_t - \nabla^2)\theta_1 = u_{x1}$. We neglect the decaying complementary function and retain only the particular integral. Thus $\theta_1 = u_{x1}/(k^2 - \mathrm{i}\omega)$, for each of the three wave components introduced above. At leading order, the thermal physics is slaved to the inertial waves, but feeds back critically on the problem at higher order (via the buoyancy acceleration) to produce the convective overstability's growth (see physical arguments in Section 3.3 in L16).

A3 Solvability conditions at order ϵ^2

At the next order the Navier–Stokes equation can be boiled down to the relatively simple

$$\mathcal{L}u_{x2} = \partial_z^2\partial_t N_x + 2\partial_z^2 N_y - \partial_{xzt} N_z, \tag{A5}$$

where the right-hand side terms involve only solutions of the preceding order and are written using

$$\mathbf{N} = -\partial_T \mathbf{u}_1 - \mathbf{u}_1 \cdot \nabla \mathbf{u}_1 + r\mathbf{e}_x\theta_1 + p\nabla^2\mathbf{u}_1.$$

A solvability condition for equation (A5) is that the right-hand side possesses no component proportional to the eigenfunctions of $\mathcal{L}$, i.e. E_A, E_B, and E_C, in our problem. To ensure this, we simply zero the coefficients of these three factors, recognizing that $E_B^* E_C = E_A e^{-\mathrm{i}\delta T}$, $E_A E_B = E_C e^{\mathrm{i}\delta T}$, and $E_A^* E_C = E_B e^{-\mathrm{i}\delta T}$. Doing so obtains three evolution equations for the mode amplitudes A, B, and C:

$$\frac{\mathrm{d}A}{\mathrm{d}T} = (\sigma_A - p)A + \mathrm{i}c_1 B^* C\, e^{-\mathrm{i}\delta T}, \tag{A6}$$

$$\frac{\mathrm{d}B}{\mathrm{d}T} = (\sigma_B - pk_B^2)B - \mathrm{i}c_2 A^* C e^{-\mathrm{i}\delta T}, \tag{A7}$$

$$\frac{\mathrm{d}C}{\mathrm{d}T} = (\sigma_C - pk_C^2)C + \mathrm{i}c_3 A B e^{\mathrm{i}\delta T}. \tag{A8}$$

Here the linear terms combine (i) the asymptotic COS growth rates of each mode in the limit of small R (see Section 3.1 in L16), i.e. $\sigma_A = \frac{1}{4}r(1+\mathrm{i})$, $\sigma_B = \frac{1}{2}r\omega_B^2/(k_B^2 - \mathrm{i}\omega_B)$, and $\sigma_C = \frac{1}{2}r\omega_C^2/(k_C^2 - \mathrm{i}\omega_C)$, and (b) the viscous damping terms proportional to p. Note that for modes B and C the viscous damping easily dominates the growth due to the COS (which can be omitted), while in mode A we can control the rate of COS growth via the size of $\frac{1}{4}r - p$.

Expressions for the non-linear coefficients are

$$c_1 = \frac{k_x\left[\omega_B(2+\omega_B) + n(2\omega_B^2 + 2\omega_B - 1)\right]}{2n(1+n)\omega_B(1+\omega_B)}, \tag{A9}$$

$$c_2 = \frac{k_x\omega_B\left[(k_B^2+2n)\omega_B^2 + (k_B^2+n)\omega_B + n^2\right]}{2n(1+n)(1+\omega_B)}, \tag{A10}$$

$$c_3 = -\frac{k_x\omega_C\left[(k_B^2-1)\omega_B^2 + (k_B^2-n-2)\omega_B + n(n+1)\right]}{2n(1+n)\omega_B}, \tag{A11}$$

where we recall that $\omega_B = -n/k_B$, $k_B = \sqrt{n^2 + k_x^2}$, $\omega_C = 1 + \omega_B$, and n and k_x are related via the leading order resonance condition equation (A4). For the first few resonances we consider, $c_i > 0$. Note that the detuning introduces extra complex exponential factors into the quadratic terms.

A4 Simplifications, rescalings, and analysis

For the rest of the appendix we omit the subdominant growth rates of the B and C modes, i.e. σ_B and σ_C. These have little to no impact on the dynamics. Also to simplify the equations somewhat, without altering their main features, we set $k_C = k_B$, and thus the damping rate of the two daughter modes are the same.

A4.1 Energetics and parametric instability

Though the system is open, the non-linear transfer terms must conserve the kinetic energy $K = \frac{1}{2}(|\mathbf{u}_A A|^2 + |\mathbf{u}_B B|^2 + |\mathbf{u}_C C|^2)$. On differentiating K with respect to T and using equations (A6)–(A8), but only with the non-linear terms active, we obtain the identity $c_1|\mathbf{u}_A|^2 - c_2|\mathbf{u}_B|^2 - c_3|\mathbf{u}_C|^2 = 0$, which provides a useful check on the algebraic expressions for the c_i. It follows that the total energy of the system is controlled by the linear terms, namely energy input by the primary COS mode (A) and viscous dissipation of the two daughter modes (B and C):

$$\frac{\mathrm{d}K}{\mathrm{d}T} = (\tfrac{1}{4}r - p)|\mathbf{u}_A A|^2 - pk_B^2(|\mathbf{u}_B B|^2 + |\mathbf{u}_C C|^2).$$

For a quasi-steady state the right-hand side need not be zero (for most of the oscillations we find it varies between positive and negative values), but it must integrate to zero on sufficiently long times or over the period of a cycle.

In the case of a constant A and an exact resonance ($\delta = 0$), equations (A6)–(A8) provide the growth rate of the parametric instability discussed earlier; it is simply $\sqrt{c_2 c_3}|A|$. This expression agrees with the growth rate derived in L16 once it is recognized that we can identify $|A| = 4S$: in L16 a real standing wave was used for the primary while in this paper we have assumed that the primary is a complex traveling wave.

A4.2 Simplified, rescaled system

The dynamical system can be simplified by the following transformation:

$$A \to \frac{pk_B^2 A}{\sqrt{c_2 c_3}}, \quad B \to \frac{\mathrm{i}pk_B^2 B}{\sqrt{c_1 c_3}}, \quad C \to \frac{pk_B^2 C}{\sqrt{c_1 c_2}}, \quad T \to \frac{T}{pk_B^2}.$$

We then obtain

$$\frac{\mathrm{d}A}{\mathrm{d}T} = \lambda A + B^* C\, e^{-\mathrm{i}\bar{\delta}T}, \quad \frac{\mathrm{d}B}{\mathrm{d}T} = -B - A^* C e^{-\mathrm{i}\bar{\delta}T}, \tag{A12}$$

$$\frac{\mathrm{d}C}{\mathrm{d}T} = -C - AB e^{\mathrm{i}\bar{\delta}T}, \tag{A13}$$

where the scaled primary's growth rate is $\lambda = (\sigma_A - p)/(pk_B^2)$ and the scaled detuning factor is $\bar{\delta} = \delta/(pk_B^2)$. The time-scale of the new system is pinned to the (fast) viscous decay of the daughter modes, against which the primary's growth may be considered slow.

For λ real, this system has enjoyed considerable attention, most notably in Vyshkind and Rabinovich (1976), Wersinger et al. (1980), Bussac (1982a, b), and Hughes and Proctor (1990, 1992), who plot out its various behaviours and bifurcations. Aside from plasma physics, where the system first appeared, analogous dynamics in astrophysics occurs in the 'r-mode instability' in neutron stars, where an unstable Rossby wave transfers its energy to other smaller scale inertial waves (Arras et al. 2003), and in overstable gravity modes in ZZ Ceti stars (Wu and Goldreich 2001), amongst other applications (Moskalik 1985). In addition to unbounded solutions, the system exhibits a range of sometimes chaotic oscillations, some akin to predator-prey bursts (combining the slow and fast time-scale), and others far more regular. In the following, we briefly describe the main features of these behaviours, as they impact on our particular system.

A4.3 Amplitude-phase dynamics and their fixed points

Equations (A12)–(A13) appear to be sixth order but can be reduced to a third-order system. First, it is easy to show that $||C|^2 - |B|^2| \propto \exp(-2T)$, and thus on the longer time-scales of interest the moduli of the two daughter modes are the same. We hence set $|B| = |C|$ and derive the following evolutionary equations:

$$\dot{a} = \lambda_r a + b^2 \cos\psi, \qquad \dot{b} = -b - ab\cos\psi, \tag{A14}$$

$$\dot{\psi} = \bar{\delta} + \lambda_i + \frac{2a^2 - b^2}{a}\sin\psi, \tag{A15}$$

where an overdot signifies a T derivative, $a = |A|$, $b = |B|$, and $\psi = \mathrm{Arg}(A) + \mathrm{Arg}(B) - \mathrm{Arg}(C) + \bar{\delta}\,T$ (Vyshkind and Rabinovich 1976). A feature that distinguishes our equations from those derived in other physical applications is the imaginary part of the growth rate λ_i, which functions as an additional detuning.

These equations support two fixed points, the trivial state $a = b = 0$ of Keplerian shear, which we know is convectively overstable, and a second state determined from

$$\psi = \tan^{-1}\left(\frac{\bar{\delta} + \lambda_i}{2 - \lambda_r}\right), \quad a = -\sec\psi, \quad b^2 = \lambda_r \sec^2\psi,$$

in which ψ must lie in the 2nd or 3rd quadrant. Though it appears as a fixed point in the amplitude-phase dynamics, in (A, B, C) space, this invariant object corresponds to an orbit of constant $|A|$, $|B|$, and $|C|$, with a fixed kinetic energy.

The linear stability of this non-trivial fixed point is straightforward to check. Skipping all the algebra (see Wersinger et al. 1980, Hughes and Proctor 1990), we find that we have stability for sufficiently large detuning:

$$\bar{\delta} + \lambda_i > |2 - \lambda_r|\sqrt{\frac{\lambda_r^2 - 2\lambda_r + 2}{2 - 2\lambda_r - \lambda_r^2}}, \tag{A16}$$

and as long as $\lambda_r < \sqrt{3} - 1$. To leading order in small λ_r, the stability criterion simplifies to $\bar{\delta} + \lambda_i > 2$. The curve of marginal stability is plotted in Fig. A1.

As we decrease $\bar{\delta}$ and pass through the critical stability threshold (A16), the fixed point undergoes a Hopf bifurcation and at first is encased in a stable limit cycle. As $\bar{\delta}$ and/or λ_r decreases the cycle undergoes a sequence of period-doubling bifurcations and then transitions to a set of mildly chaotic relaxation oscillations. On the other hand, when $\lambda_r > \sqrt{3} - 1$ the fixed point is subject to a monotonically growing instability and the system tends to blow up. For a fuller account of these dynamics, the reader is directed to the numerical surveys described in Vyshkind and Rabinovich (1976), Wersinger et al. (1980) and Bussac (1982a), and their analytic reduction to simple 1D maps, such as in Bussac (1982b) and Hughes and Proctor (1990, 1992). Note that on account of the non-negligible imaginary part of the COS's growth rate (which acts as an additional detuning), the dynamics we witness never plunge into the full bouts of chaos some of these authors discover.

Before moving on, a final point worth making is that, even if unstable, the fixed point above organizes the dynamics and to some extent determines the mean amplitude of the non-linear saturation. As all the parameters that appear in the above analysis are order one or small, we obtain $a \sim 1$ at saturation, which (for $n = 1$) yields $|\mathbf{u}'| \sim \epsilon p k_B^2 \sim \mathrm{Pr}\, k_B^2 \approx 7R$, where we note that $k_B^2 \approx 7$ for $n = 1$. This estimate is similar, if slightly larger, than the saturation estimate given in L16 when adopting a 'parasitic theory'. It thus extends and places such a theory on a sounder footing, at least in the regime of near criticality.

A5 Illustrative solutions

To give a flavour of the types of behaviour exhibited near COS criticality, we numerically solve equations (A12)–(A13) for fixed $n = 1$ but different r/p and $\bar{\delta}$, the two main control parameters. For this choice of resonance, $k_x = 2.49$ and thus $c_1 = 5.52$, $c_2 = 0.287$, $c_3 = 1.36$, and $k_B^2 = 7.20$.

In Fig. A2, we plot three representative solutions. In the left-hand panels we set $r/p = 8$ (thus $\lambda = 0.139 + 0.278$i) and adopt a moderate level of detuning $\bar{\delta} = 2$. The fixed point in this case is a stable focus, and after an initial transient the system spirals on to it, as illustrated in the bottom left phase portrait. In the middle plots we retain the same r/p but reduce the detuning so that $\bar{\delta} = 1$; as predicted, the fixed point is now unstable but centres a stable limit cycle that controls a regular non-linear oscillation, with the primary mode and the daughter modes somewhat out of phase. The predator–prey alluded to in these dynamics is brought out best at lower r/p and $\bar{\delta}$, and we show this in the right-hand panels, for which $r/p = 4.2$ (thus $\lambda = 0.00694 + 0.146$i) and $\bar{\delta} = 0$. Here in the upper panel we witness bursty dynamics comprising the slow exponential growth of the primary, and its abrupt destruction by the parasitic daughter modes on a much faster time-scale. Once they dissipate, the primary is free to grow again and the cycle repeats. Similar behaviour is exhibited in several biological systems involving multiple predators (e.g. Muratori and Rinaldi 1989), and in the net-vertical-flux MRI near criticality (Latter et al. 2009, Lesaffre et al. 2009). These 'fast-slow' dynamics may be captured by a two-scale formalism, as in Hughes and Proctor (1990, 1992), though we decline to engage with that here. Of interest, however, is the somewhat chaotic nature of the relaxation oscillation, best illustrated in the lower right-hand panel: there is no stable limit cycle, but rather a strange attractor which imparts some disorder to the various peaks of $|A|$, though this variability is rather minor in this case, and not evident in the top right-hand panel.

APPENDIX B: MEAN FIELD MODEL OF ZONAL FLOW FORMATION

Here we provide a somewhat more quantitative approach to the process described in Section 6, by developing a crude mean field model, in a similar spirit to Garaud and coworkers (see also Frisch 1989, and Latter and Balbus 2012).

B1 Preliminaries

We are mostly concerned with the angular momentum in our local model, which corresponds to the canonical y-momentum: $h = 2\Omega x + u_y$. It obeys the conservation equation:

$$\partial_t h + \nabla\cdot(h\mathbf{u} - \nu\nabla h) = 0. \tag{B1}$$

In laminar equilibrium $u_y = -q\Omega x$ and thus $h = h_0 = (2 - q)\Omega x = [\kappa^2/(2\Omega)]x$. Clearly, the angular momentum increases outwards (at least for $\kappa^2 > 0$ as assumed here), and the disc is Rayleigh stable.

In addition, it is useful (though not necessary) to consider the total buoyancy in the shearing box: $\theta_x = -x + \theta$, which obeys our other conservation equation:

$$\partial_t\theta_x + \nabla\cdot(\theta_x\mathbf{u} - \xi\nabla\theta_x) = 0. \tag{B2}$$

Recognizing that $\theta = -(\partial_Z S)_0^{-1} S'$, where S' is the dimensionless entropy perturbation, we identify θ_x with the total entropy in our box. In our laminar equilibrium $\theta_x = \theta_{x0} = -x$, and thus the entropy decreases outwards, indicating the disc is Schwarzchild unstable.

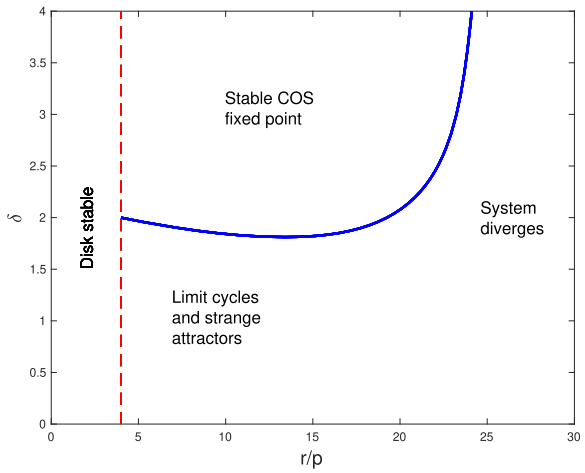

Figure A1. Following Bussac (1982a), the basic structure of the dynamical system as described in the $(r/p,\ \bar{\delta})$ parameter plane for a $n = 1$ resonance.

The R parameter, the determinant of COS instability and strength, can hence be generalized to a space (and time dependent) quantity, sensitive to the particulars of the turbulence at any location and how effectively it has counteracted the equilibrium gradients presented above. We define

$$R_{\rm eff} = \frac{N^2(\partial\theta_x/dx)}{2\Omega(\partial h/\partial x)}, \tag{B3}$$

which returns to $R_{\rm eff} \equiv R_0 = -N^2/\kappa^2$, in our basic state, as required.

B2 Turbulent fluctuations and mean field equations

Suppose the COS grows and saturates in inertial wave turbulence, characterized by short length and time-scales, x and t, etc. Let us consider long radial wavelengths and slow temporal variations atop these fluctuations using the slow radial and temporal variables X and T, so that $h = h(x,\ z,\ t,\ X,\ T)$ and $\theta_x = \theta_x(x,\ z,\ t,\ X,\ T)$. Next we introduce an averaging procedure over intermediate radial and time-scales and all vertical scales, $\langle\ \cdot\ \rangle_{x,\,z,\,t}$, which removes the small-scale fluctuations and thus isolates mean components H and Θ, so that

$$H(X,T) \equiv \langle h(x,z,t,X,T)\rangle_{x,z,t},$$
$$\Theta(X,T) \equiv \langle \theta_x(x,z,t,X,T)\rangle_{x,z,t},$$

these can then be used to define an additional fluctuating part to h and θ_x, which we denote with primes, and which average to zero. It is next assumed that there is no appreciable mean radial velocity, which may be justified if we take the mean quantities to be generally small in amplitude. Note that the averaging retains the laminar equilibrium background, so that H includes the component $\kappa^2/(2\Omega)X$ and Θ the component $-X$. Finally, we adopt units so that $\Omega = 1$ and $\sqrt{\xi/\Omega} = 1$.

The mean conservation laws for angular momentum and entropy are hence:

$$\partial_T H + \partial_X\left(F_H - \Pr\,\partial_X H\right) = 0, \tag{B4}$$

$$\partial_T \Theta + \partial_X\left(F_\Theta - \partial_X \Theta\right) = 0, \tag{B5}$$

where Pr is the (small) Prandtl number, the angular momentum flux is $F_H = \langle u_x' p_y'\rangle_{x,z,t}$, in other words the Reynolds stress, and the thermal flux is $F_H = \langle u_x'\theta_x'\rangle_{x,z,t}$.

From our numerical experience, the turbulent thermal flux F_Θ is usually much smaller than the laminar radiative flux and if dropped permits the two equations to decouple. Then Θ obeys the diffusion equation on short time-scales – short at least compared to the angular momentum evolution – and the Θ dynamics can be justifiably neglected, though we retain them for the moment. In equation (B4), however, both the Prandtl number and turbulent fluxes are small and can be comparable. They are thus both retained.

We next assume that $F_H < 0$ and $F_\Theta > 0$. But to make progress, we need to introduce a closure scheme. Noting that the turbulent fluxes depend on the local turbulent strength, which in turn depend

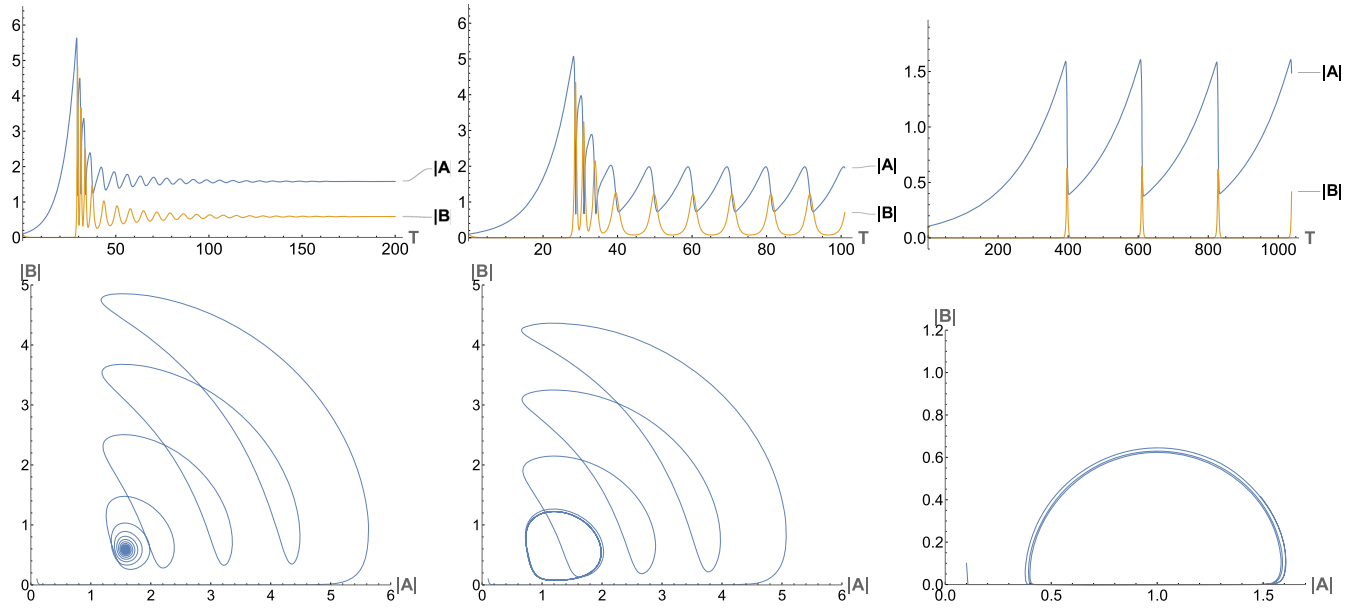

Figure A2. Three numerical examples of different dynamical behaviours. In the left-hand column we plot a solution associated with the parameter set $r/p = 8$ and $\bar{\delta} = 2$, with the time evolution of the wave amplitudes on the top, and their phase portrait on the bottom. The middle column corresponds to $r/p = 8$ and $\bar{\delta} = 1$, and the right-hand column to $r/p = 4.2$ and $\bar{\delta} = 0$.

on the magnitude of R, we set $F_H = F_H(R_{\rm eff})$ and $F_\Theta = F_\Theta(R_{\rm eff})$, where in the mean field setting and in our adopted units we have $R_{\rm eff} = -R_0(\partial\Theta/dX)/(2\partial H/\partial X)$. Finally we define

$$R_0\left(\frac{{\rm d}F_H}{{\rm d}R_{\rm eff}}\right)_0 \equiv F'_H < 0, \qquad R_0\left(\frac{{\rm d}F_\Theta}{{\rm d}R_{\rm eff}}\right)_0 \equiv F'_\Theta > 0.$$

B3 Linear stability of homogeneous turbulence

Consider the state of (quasi-) steady homogeneous COS wave turbulence in a Keplerian disc. The mean fields hence comprise only the background laminar gradients, so that $H = H_0 = (1/2)X$ and $\Theta = \Theta_0 = -X$.

We next disturb this background with mean perturbations H' and Θ'. It can be quickly shown that these give rise to a perturbation in the R parameter, which to linear order is $R'_{\rm eff} = -R_0(2\partial_X H' + \partial_X\Theta')$. We may then write down the coupled linearized equations for the two perturbations:

$$\partial_T H' = ({\rm Pr} + 2F'_H)\partial_X^2 H' + F'_H\partial_X^2\Theta', \tag{B6}$$

$$\partial_T \Theta' = (1 + F'_\Theta)\partial_X^2\Theta' + 2F'_\Theta\partial_X^2 H'. \tag{B7}$$

If we assume, as mentioned earlier, that the thermal fluctuation will be smeared out rapidly by radiative diffusion, then we can drop the last term on the right in equation (B6). This then yields the diffusion equation with transport coefficient ${\rm Pr}+2F'_H$. If this is positive then the disturbance decays, but if it is negative then we have antidiffusion and the formation of layers of high and low angular momentum. As a consequence, the criterion for instability is simply that viscous diffusion is sufficiently weak ${\rm Pr} < -2F'_H$ (noting that $F'_H < 0$) and fails to remedy the sharpening of gradients brought about by the turbulent flux.

Incorporating the thermal dynamics now, we obtain a dispersion relation for normal modes of the type $\propto e^{sT + {\rm i}KT}$:

$$s^2 + K^2(1 + F'_\Theta + 2F'_H + {\rm Pr})s + K^4\left[2F'_H + {\rm Pr}(1 + F'_\Theta)\right] = 0, \tag{B8}$$

and the instability criterion is modified slightly:

$${\rm Pr} < \frac{-2F'_H}{1 + F'_\Theta}.$$

Thus the thermal physics is somewhat stabilizing.

This paper has been typeset from a TEX/LATEX file prepared by the author.